DESIGN AND SIMULATION OF AN AUSCULTATION DATA ACQUISITION SYSTEM ON A SINGLE INTEGRATED CHIP

by

Kerem Kaya

B.S., Electrical and Electronics Engineering, Boğaziçi University, 2019

Submitted to the Institute for Graduate Studies in
Science and Engineering in partial fulfillment of
the requirements for the degree of
Master of Science

Graduate Program in Electrical and Electronics Engineering
Boğaziçi University

2022

ACKNOWLEDGEMENTS

I would like to thank my supervisor Prof. Yasemin Kahya for her immense support and development on my academic and personal life. You were there and always helping me whenever I had a problem. Frankly, I am sad that I was not always there and left things in half. I am really happy to working with you on such a good project with a noble impact and have a good thesis (I hope) to help.

I would like to thank my co-supervisor Prof. Günhan Dündar for his support throughout all of my academic career. I mean it would be impossible to finish this thesis without learning from your immense knowledge and experience. I am really glad to take all of your courses and learn as much as I can. My greatest goal would be a person like you.

I would like to thank Kemal Ozanoğlu, PhD and the team, Assist. Prof. Okan Zafer Batur, Alper and Sedat for being my mentor on this project nearly every week. During long hours of frustration and uncertainity, you had a good answer and we solved them. I think I am slowly understanding what does it mean to be a good engineer in a really good team and I am sure that this team will make much much more. I would like to thank Assist. Prof. İpek Şen for her kindness and support on my time around. You are really a good teacher, thanks to you I can understand how a machine learns its way. I would like to thank all of my coworkers, Onur, Çağlayan, Metehan, Şiyar and Mehmet Kahya at Electrosalus. I had wonderful time working together with you, hope you also had the same.

I want to thank those wonderful people, Mücahit, Mukadder and Ceren. It was not going to be better, much worse if you were not my family and at my side. I am grateful that all of you are being with me.

I would like to express my gratitude to my partner in crime, the most joyful person in the world, Müge. Thanks for being by my side, making everything much much more enjoyable and all your immense support. You have been the sunshine of my life since 2013. All this would definitely not be possible without your assistance and love. I am so lucky to be with an amazing one like you.

ABSTRACT

DESIGN AND SIMULATION OF AN AUSCULTATION DATA ACQUISITION SYSTEM ON A SINGLE INTEGRATED CHIP

The COVID-19 pandemic has reminded us of the importance of remote healthcare and early detection of symptoms, as most healthcare systems cannot accommodate all patients at once. The burden on health systems can be reduced with smart wearable remote sensing technologies and online health services. This study aims to design a wearable auscultation data acquisition system on a single integrated chip for remote health monitoring. In this study, available auscultation devices, from a conventional stethoscope to multi-channel computerized data acquisition systems, were carefully investigated. The current standard in computerized auscultation data acquisition systems was analyzed and the design choice for a sound acquisition system was presented. The use of low current consuming, high performance MEMS microphone systems has been listed in other wearables in terms of active noise cancellation and as a potential candidate for the proposed low-power wearable auscultation sensor interface. The versatile switched-capacitor-based gain stage and second-order filter design is quickly implemented with Python support. In order to place the other building blocks of the designed new auscultation data acquisition system in a single system, the post-layout simulation of the switched capacitor filter blocks was made using TSMC 180 nm technology, and an important progress is made in development of the proposed system in a single integrated chip.

ÖZET

BİR STETOSKOP SES VERİSİ EDİNİMİ SİSTEMİNİN TÜMLEŞİK DEVRE ÜZERİNDE TASARIM VE SİMÜLASYONU

COVID-19 salgını, sağlık sistemlerinin çoğu aynı anda tüm hastalara uyum sağlayamadığı için uzaktan sağlık hizmetinin ve semptomların erken tespitinin önemini hatırlattı. Sağlık sistemleri üzerindeki yük akıllı giyilebilir uzaktan algılama teknolojileri ve çevrimiçi sağlık hizmetleri ile azaltılabilir. Bu çalışma, uzaktan sağlık izleme için tek bir entegre çip üzerinde giyilebilir bir oskültasyon veri toplama sistemi tasarlamayı amaçlamaktadır. Bu çalışmada geleneksel bir stetoskoptan çok kanallı bilgisayarlı veri toplama sistemlerine kadar mevcut oskültasyon cihazları dikkatlice araştırıldı. Bilgisayarlı oskültasyon veri toplama sistemlerindeki mevcut standart analiz edildi ve bir ses toplama sistemi için tasarım seçimi sunuldu. Az akım tüketen, yüksek performanslı MEMS mikrofon sistemlerinin kullanımı, aktif gürültü iptali açısından diğer giyilebilir cihazlarda ve önerilen düşük güçlü giyilebilir oskültasyon sensörü arayüzü için potansiyel bir aday olarak listelendi. Çok yönlü anahtarlamalı kapasitör tabanlı kazanç aşaması ve ikinci dereceden filtre tasarımı Python desteği ile hızlıca gerçeklenmiştir. Tasarlanan yeni oskülasyon veri toplama sisteminin diğer yapı taşlarını tek bir sistemde yerleştirmek için anahtarlamalı kapasitör filtre bloklarının yerleşim sonrası simülasyonu TSMC 180 nm teknolojisi kullanılarak yapılmıştır ve sistemin tek bir entegre çip haline getirilmesinde önemli bir aşama kaydedilmiştir.

TABLE OF CONTENTS

LIST OF FIGURES

LIST OF TABLES

LIST OF SYMBOLS

a_i	Transfer function coefficient
b_i	Transfer function coefficient
C_i	Capacitor
f_i	Frequency
$H_i(s)$	Transfer function in Laplace domain
K_i	Transfer function coefficeint in Laplace domain
$[n]$	Discrete time step
R_{eq}	Equivalent resistance
T	Period of a clock cycle
q_i	Charge at a node
Q_i	Charge at a node
v_i	Voltage at a node
Δq_i	Charge difference
ϕ_n	Switch clock frequency
ω_0	Pole frequency

LIST OF ACRONYMS/ABBREVIATIONS

AC	Alternating Current
ADC	Analog-to-Digital Converter
COPD	Chronic Obstructive Pulmonary Disease
CORSA	Computerized Respiratory Sound Analysis
COVID-19	Coronavirus 19
DC	Direct Current
ECM	Electret Condenser Microphone
GBW	Gain-Bandwidth Product
HPF	High Pass Filter
IC	Integrated Circuit
JFET	Junction Field Effect Transistor
LPF	Low Pass Filter
MEMS	Micro Electro Mechanical Systems
NMOS	N-Channel Metal-Oxide Semiconductor
OPAMP	Operational Amplifier
PMOS	P-Channel Metal-Oxide Semiconductor
RC	Resistor-Capacitor
SARS-CoV-2	Severe Acute Respiratory Syndrome Coronavirus 2
SciPy	Scientific Python
SNR	Signal to Noise Ratio
SPI	Serial Peripheral Interface
TSMC	Taiwan Semiconductor Manufacturing Company

1. INTRODUCTION

According to the World Health Organization [1], 6.294.969 people around the world have been reported to die because of SARS-CoV-2 so far. Getting infected with COVID-19 might be deadly, especially for certain risk groups. In the beginning of 2020, COVID-19 pandemic started to hit elderly care houses in most of the countries and they were and still are the most vulnerable ones in society. The research paper published in Italy [2] states that the elderly is the most affected group with 25.3% of total infections and 55.3% of total mortality in Italy, April 2020. As we have seen in Italy, age is one of the most prominent factors in COVID-19 besides having an existing respiratory condition. As in the case of SARS-CoV-2 virus, most of the infected people that have an existing respiratory condition or chronic obstructive pulmonary disease(COPD) faced the danger of falling severely ill. In [3], it is shown that people without COPD are likely to experience severe COVID-19 disease at 33.4% compared to patients with COPD at 63% severity risk. Moreover, at the end of the same article, these findings were indicators of higher death rates - 60% for the COVID-19 patients with COPD.

COVID-19 pandemic reminded us of the importance of remote healthcare and early detection of symptoms since most of the healthcare systems were not able to accommodate all the patients at the same time. The burden on the health care systems can be abolished by wearable disease detection technologies and online healthcare according to [4]. We still do not know exactly what will happen to an infected person's lungs after recovery and those who are at high risk groups will need to be monitored more in an efficient way. Remote monitoring after a diagnosis is a valuable tool for especially high risk groups. Current trends for remote monitoring are mostly software based [5] solutions combined with clinically relevant wearable devices.

The aim of this thesis is to lay a groundwork on a low power wearable respiratory data acquisition system that could be an effective solution for easy remote monitoring of respiratory diseases. In this thesis, I will explain:

- Devices that are traditionally used, stethoscopes, in detection and monitoring of respiratory diseases.
- Hardware recommendations of a low power noise canceling auscultation acquisition system in parts of:
  (i) Current microphone technologies and use cases in active noise cancellation.
  (ii) Recommended filter structures and design procedures.
- Switched capacitor filter implementation of the proposed novel system, layout and simulation of the filter blocks.
- Future work and design roadmap.

with the aim of realizing a low power, noise canceling respiratory auscultation data acquisition system on a single integrated chip.

2. STETHOSCOPES and ELECTRONIC STETHOSCOPES

This section is about stethoscopes that are used for diagnosis in clinics and the acoustic characteristics of such structures. Also, computerized auscultation acquisition systems, the current designs of electronic stethoscopes and standards for respiratory data acquisition will be discussed.

2.1. Stethoscope Design

According to the definition of Britannica, a stethoscope is a medical instrument used in listening to internally produced sounds from the body surface [6]. Historically, stethoscopes were tube-like structures as seen in Figure 2.1, allowing only one ear to listen. Variations of the stethoscope design with binaural tubes can be seen in Figure 2.2.

Figure 2.1. Laennec's stethoscope (1882) at Science Museum Group Collection, adapted from [7].

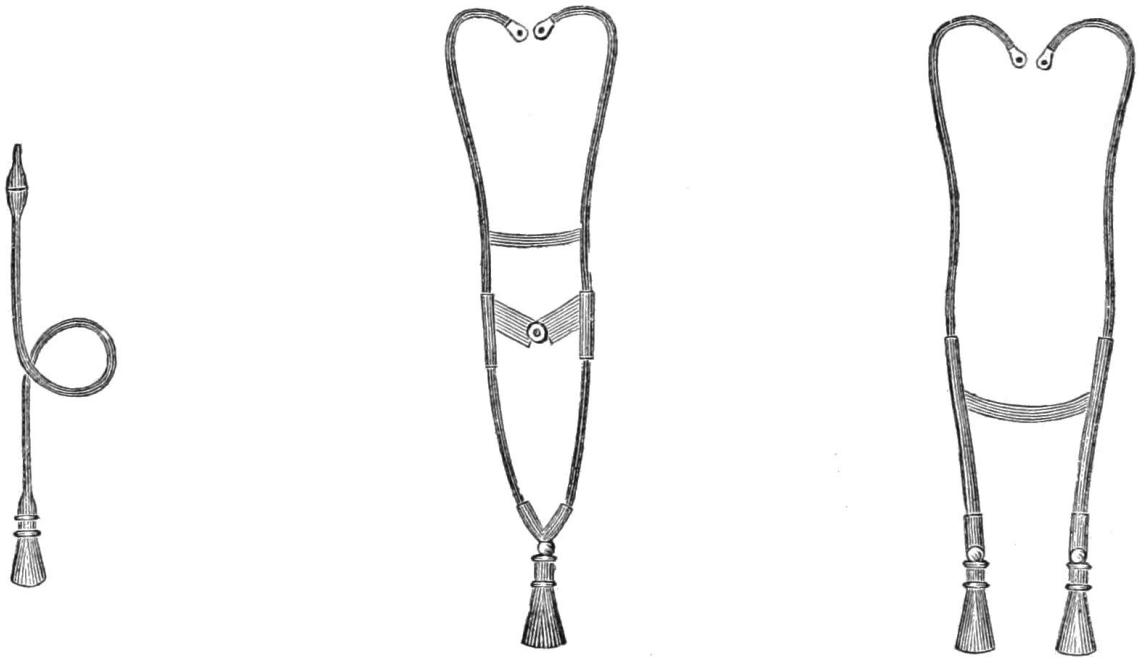

Figure 2.2. Lecture on the evolution of the stethoscope by Samuel Wilkins, adapted from [8].

A modern stethoscope consists of two tubular earpieces with a binaural connection and a piece which has a diaphragm and a bell as seen in Figure 2.3. Diaphragm and bell parts are back to back and have different frequency responses as seen in the Figure 2.4. The bell part is used for listening to low frequency sounds and the diaphragm part is used for listening to higher frequency sounds. Thus the bell attachment is more suitable for the heart related sounds and the diaphragm part is more suitable for respiratory sounds from the body [9].

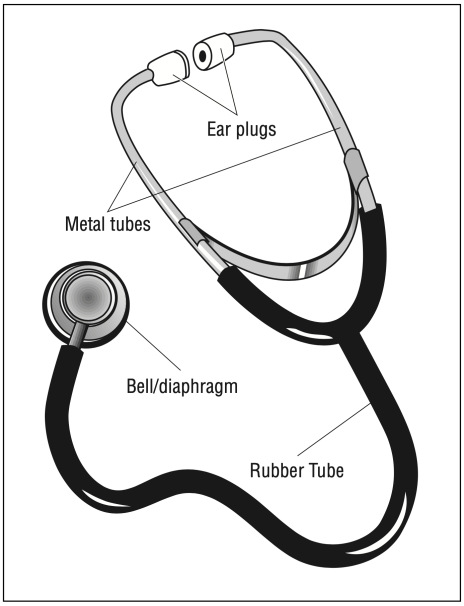

Figure 2.3. A drawing of a modern stethoscope with annotated parts, adapted from [10].

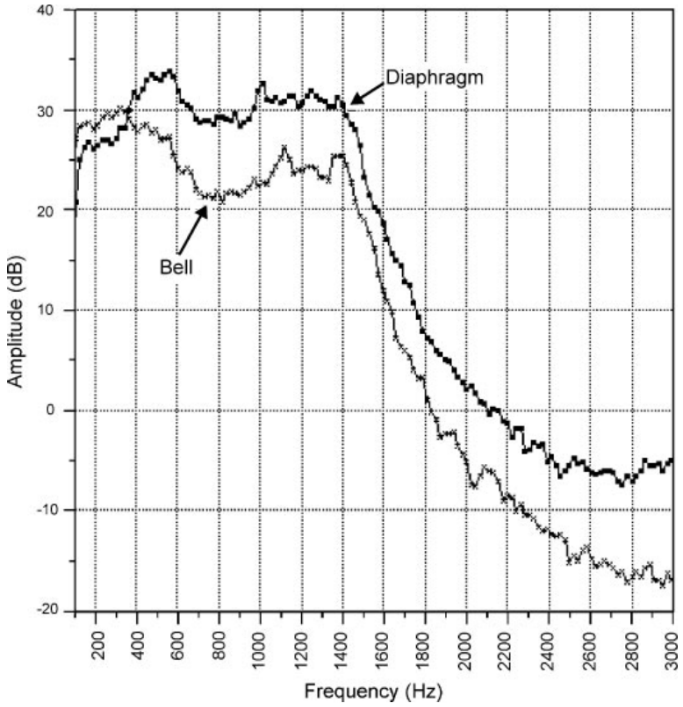

Figure 2.4. Acoustic frequency response of Littman Classic stethoscope bell and diaphragm with a white noise generator calibration system, adapted from [9].

2.2. Electronic Stethoscopes Systems and CORSA Guidelines

Clinical analysis of sound characteristics of respiratory auscultation usually leads to subjective diagnosis by just listening with a stethoscope. A doctor might hear differently from another doctor with auscultation on the same patient because of age, experience and ambient conditions. To improve that, electronic stethoscopes with amplified responses were developed to record and listen to auscultation [11–13].

Figure 2.5. A photograph of the 3M Littmann 3200 Electronic Stethoscope with electronic attachment, adapted from [13].

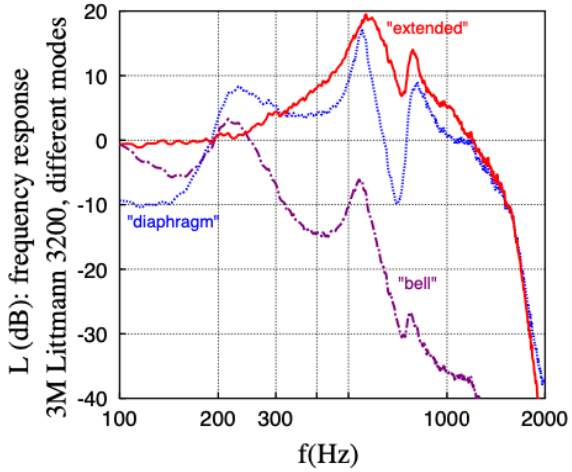

Figure 2.6. Frequency response measurements of the 3M Littmann 3200 Electronic Stethoscope with diaphragm, bell and extended modes, adapted from [14].

Most of the electronic stethoscopes do not have a flat frequency response and they usually have different filter shapes [9, 15]. A measurement result of the electronic stethoscope depicted in Figure 2.5 is presented in Figure 2.6. This leads to a prob-

lem in characterization and classification of abnormal, adventitious respiratory sounds. Adventitious respiratory sounds usually have a distinct waveform in the time domain. One of such examples is crackle sound as seen in Figure 2.7. Crackles have specific classifications according to their highest deflection highest peaks half-periods in time domain [16,17]. Any distortion in amplitude would result in a shift in half-periods and any irregular shift in time would change subsequent half-periods defined in Figure 2.7. Thus, an instrument to record such sounds should not distort its waveform both in time and frequency domain ideally [18].

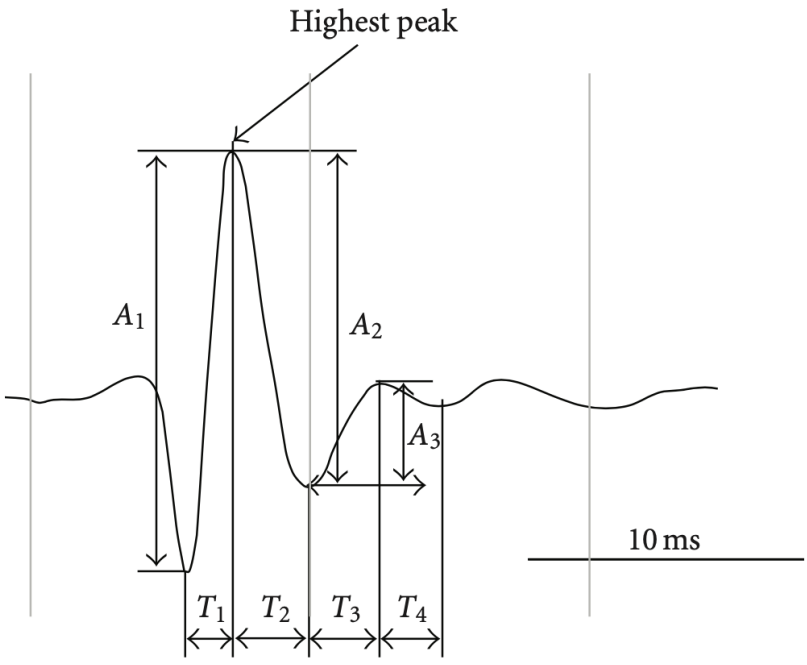

Figure 2.7. A typical waveform of a crackle. Frequency domain characteristics are classified according to their highest deflection highest peak point. Half-periods of highest deflections after polarity changes are marked as T_1, T_2, T_3 and T_4 with respect to peaks of A_1, A_2 and A_3, adapted from [16].

A European task force initiated the Computerized Adventitious Respiratory Sounds Analysis (CORSA) project to guide future researchers to have a standardized respiratory acquisition system with extensive recommendations [18–26]. Specific hardware guidelines of CORSA recommendations state that analog interface of an ideal respiratory data acquisition system essentially should have

- A sensitive sensor analog interfacing system with flat (max 6 dB deviation) frequency response from within the range of interest of respiratory sounds (30-3000 Hz) with at least 60 dB dynamic range and signal to noise ratio.
- A high pass filtering stage with linear phase, minimized ripple and a high roll off rate (18 dB/octave)
- A low pass filter with larger cut off frequency of measured signals with minimized ripple and a high roll off rate (24 dB/octave)

Different groups have demonstrated computerized auscultation acquisition systems with single or multi channel sensor systems [17,27–30]. Historically, computerized auscultation acquisition systems were stationary units coupled to a personal computer. Mobile and wearable respiratory data acquisition systems are becoming more common both in academia and the consumer market as smart stethoscope systems [11, 31–39] yet true wearable devices are not so common in terms of respiratory tracking. The recent examples of wearable devices that use a sensor for respiratory data tracking can be considered as mechano acoustic sensors [40] and sensors that combine bioelectric signals with respiratory functions. [31, 39, 41, 42] Another interesting application of vascular monitoring via a flexible microphone array is also related [43]. Most of these devices employ single or localized sensors on a fixed area of the body. A novel approach would be a sensor array that can use benefits of multi channel recording [17] capabilities such as active acoustic noise canceling with lightweight sensors that can be truly wearable. In the next section, an overview of such respiratory acquisition devices will be presented.

3. OVERVIEW of HARDWARE BLOCKS

This section consists of details of a proposed hardware solution for the low power, wearable respiratory data acquisition system with application specific integrated circuit. A preliminary overview of the proposed respiratory data acquisition system design is presented in Figure 3.1. The system consists of critical analog and digital sub-blocks. The system needs to sense auscultation signals with great sensitivity. After sensing and amplification, a series of filters are applied to remove unwanted frequencies and noise. Then signals are digitized and transmitted to a computation environment where auscultation data are stored. Depending on the application, users either listen to acquired sound in real time or analyze data later to detect anomalies and classify. The focus of this thesis will be on the microphone system with capsule and analog acquisition and filtering of sound signals.

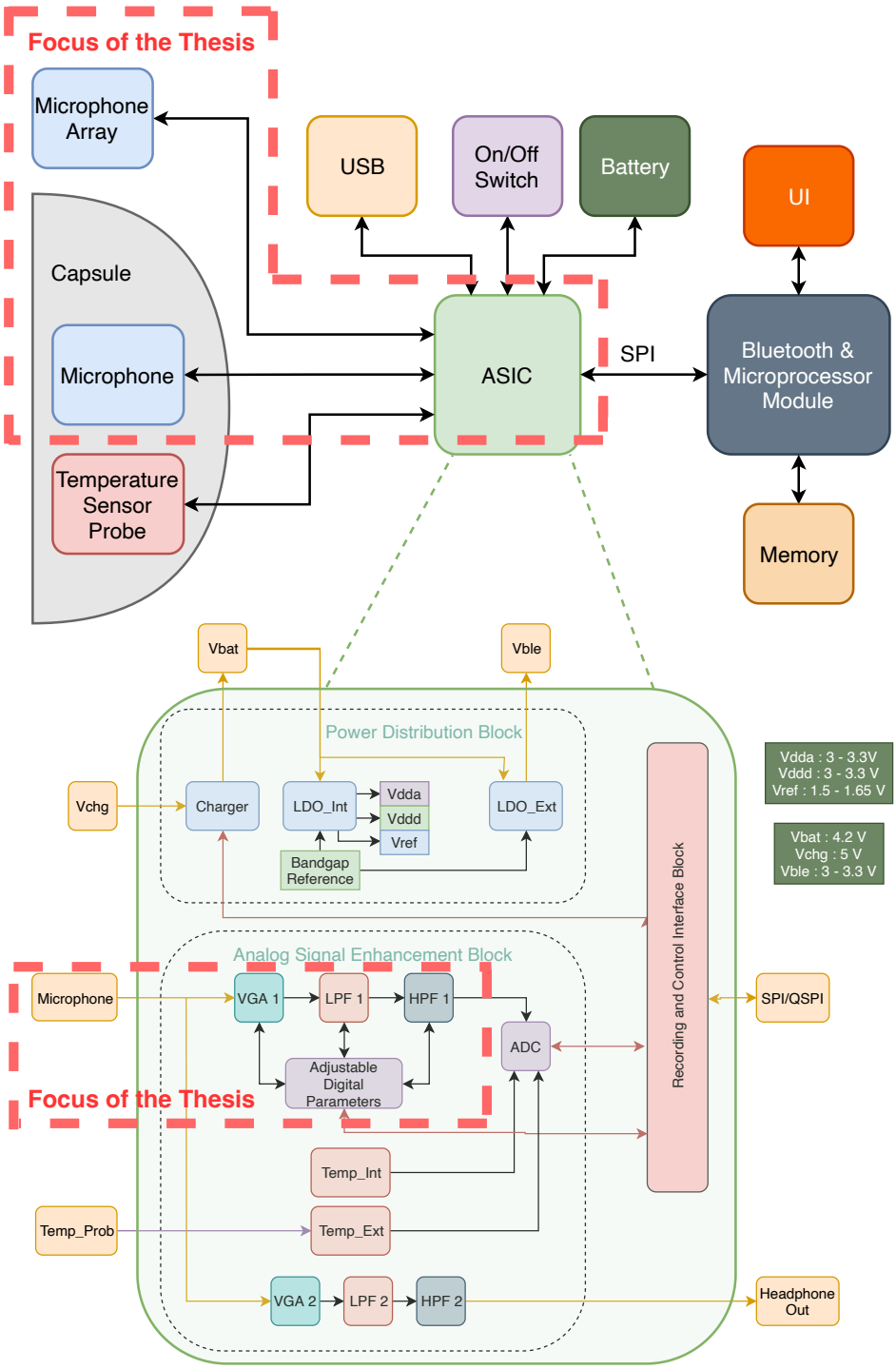

Figure 3.1. An overview of the proposed respiratory data acquisition system with the parts that constitute the main focus of this thesis.

3.1. Sensing and Amplification

3.1.1. Microphone Overview

In this section I will explain the current overview of microphone designs and a review of microphones that are commercially available for small integrated systems A microphone is a transducer that converts sound pressure difference to an electrical signal [44]. There are different types of microphones such as electret condensers and MEMS microphones. Internal structure diagrams and sensing elements of electret condenser are shown in Figure 3.2.

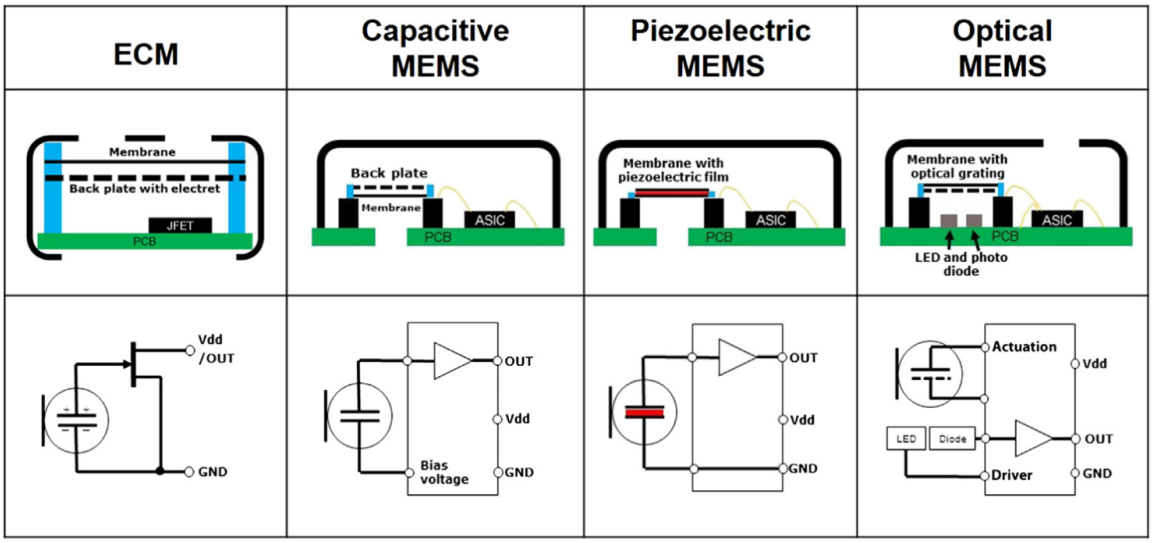

Figure 3.2. An overview of electret condenser and MEMS microphones with diagrams, adapted from [45].

In an electret condenser microphone, a charged membrane translates mechanical vibration as capacitance change on a dc biased JFET. This capacitance change can be sensed as a continuous current from the output of the electret microphone. In a MEMS microphone, silicon micromachined plate structure resonates with respect to the sound mechanically.

An integrated circuit amplifies these mechanical vibrations and depending on the type of MEMS microphone, the sound signal can be sensed as an analog voltage or can be a digital code readout. MEMS microphones are manufactured with a clean room process with better matching than electret ones. Also, they are significantly smaller than electret microphones and consume less power. Due to these advantages MEMS microphones increased their market share from 10% to 90% since 2007 [45].

MEMS microphones are heavily used in smartphones, home assistant devices, noise canceling headphones and true wireless earbuds as seen in Figure 3.3. As seen in Figure 3.4 a MEMS microphone is placed in front of the speaker driver so that both music and noise in the ear canal is recorded to be calculated in active noise canceling blocks. Different MEMS microphones in the device also can be seen in Figure 3.5.

Figure 3.3. An Apple Airpods Pro true wireless headset piece with ear cover removed, adapted from [46].

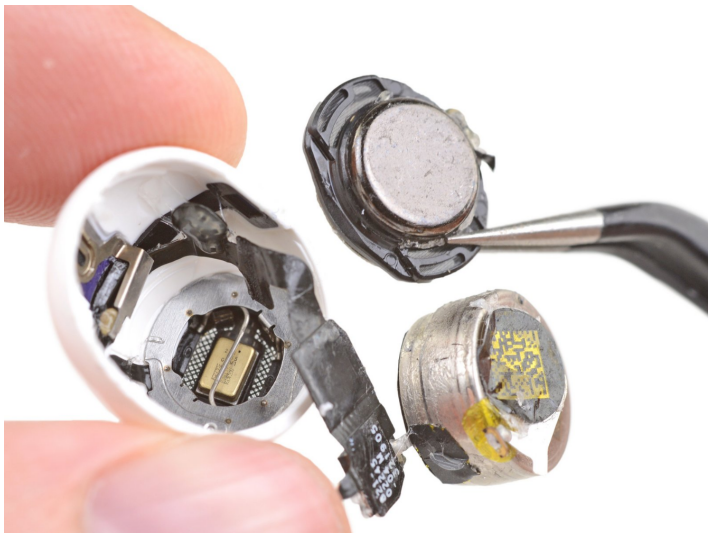

Figure 3.4. A MEMS microphone to listen ear canal that is used in adaptive noise canceling, adapted from [46].

Figure 3.5. Onboard MEMS microphones, marked in red, in one of the disassembled earpiece to be used in voice and ambient noise pickup, adapted from [46].

Electret microphones have an advantage of better frequency response than MEMS microphones since there is no moving mechanical silicon mass. However, new variants of MEMS microphones improved significantly and now they have a flat response at respiratory sound frequencies (30-3000 Hz). An example can be seen in Figure 3.6.

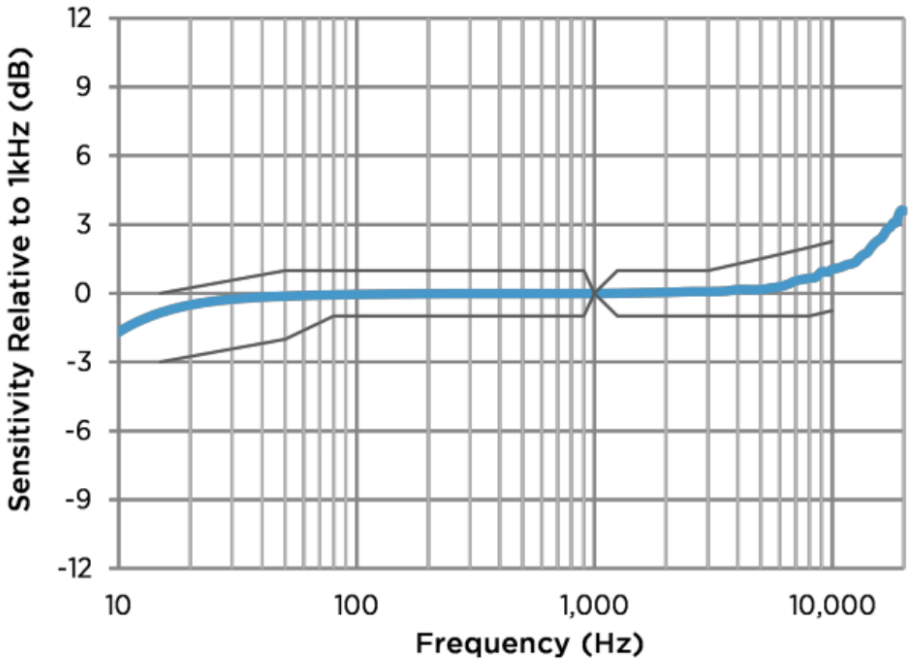

	15	50	80	900	1000	1250	3000	5000	8000	10000
USL	0	1	1	1	0	1	1	1.5	2	2.25
LSL	-3	-2	-1	-1	0	-1	-1	-1	-1	-0.75

Figure 3.6. An example of current MEMS analog microphone frequency response with 3 dB variation in 10-10000 Hz range, adapted from the datasheet of SPH8878LR5H-1 (Knowles) [47].

3.1.2. List of MEMS Microphones

According to CORSA guidelines on sensing, new analog MEMS microphones are suitable for a respiratory acquisition application where an active noise canceling application is desired.Table 3.1 shows a list of new MEMS microphones that have an analog signal output, at least minimum 20 Hz-10 kHz frequency range and 59 dB SNR and a maximum of 250 μA current consumption.

Table 3.1. Table for suitable MEMS microphones for CORSA guidelines.

Device Code	**Current**	**Range**	**Sensitivity**	**SNR**	**Ref**
ICS-40300	250 μA	6 Hz - 20 kHz	-45dB ±2dB	63dB	[48]
SPH8878LR5H-1	250 μA	7 Hz - 36 kHz	-44dB ±0.5dB	67dB	[49]
SPH1878LR5H-C	250 μA	7 Hz - 36 kHz	-44dB ±0.5dB	67dB	[50]
SPV08A0LR5H-1	200 μA	20 Hz - 10 kHz	-42dB ±1dB	64dB	[51]
CMM-2718AB-3815	170 μA	20 Hz - 10 kHz	-38dB ±1dB	62dB	[52]
SPH1878LR5H-1	220 μA	10 Hz - 10 kHz	-38dB	66dB	[53]
CMM-2718AT-3817	175 μA	20 Hz - 10 kHz	-38dB ±1dB	64dB	[54]
AMM-2742-T-R	150 μA	20 Hz - 20 kHz	-42dB ±1dB	59dB	[55]
AMM-3742-T-WP-R	200 μA	20 Hz - 20 kHz	-42dB ±1dB	59dB	[56]

3.1.3. Air Coupling and Acoustics

Computerized respiratory signal acquisition systems that use microphones either use a contact microphone, similar to membrane based electronic stethoscopes [57] or use air coupled microphones with a specific cavity geometry and material to maximize acoustic conduction as seen in as seen in Figure 3.7 and Figure 3.8 [9, 17, 58].

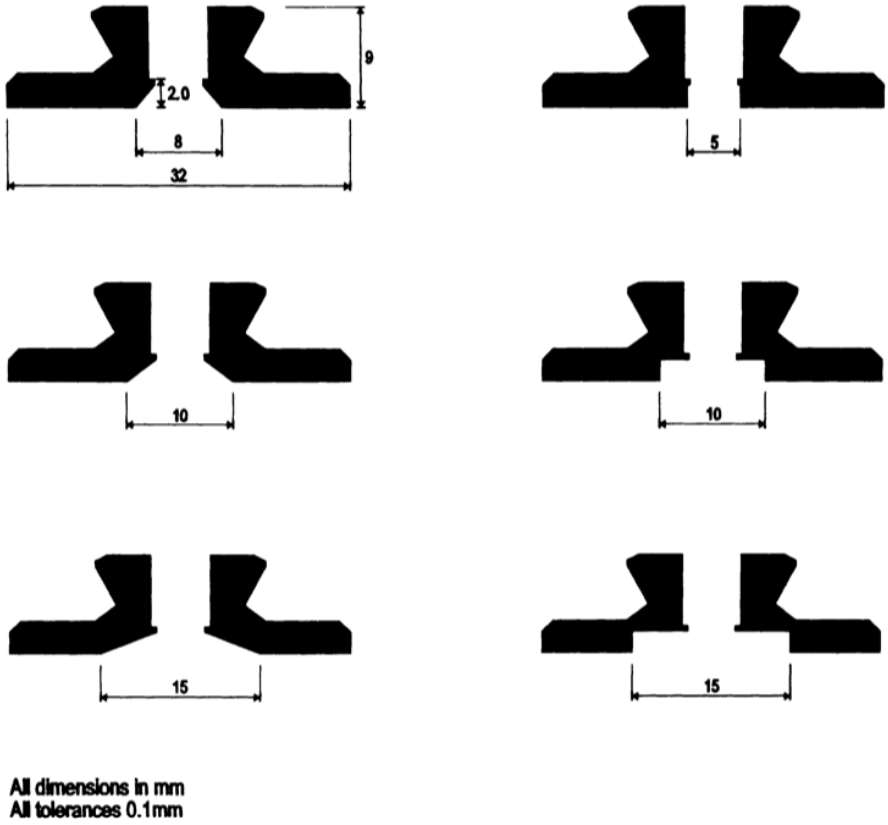

Figure 3.7. Different air coupler geometries before electret microphone insertion, adapted from [59].

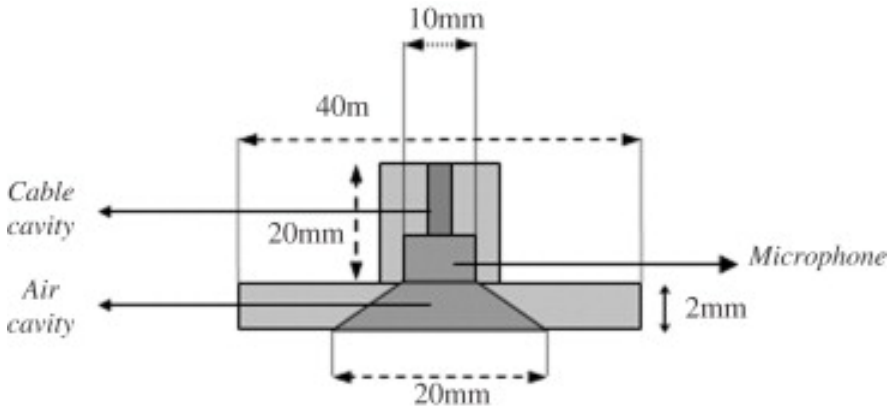

Figure 3.8. Teflon capsule used with Sony ECM 44BPT electret microphone at Lung Acoustics Laboratory, adapted from [58].

For a MEMS microphone system, this acoustic air interface needs to be analyzed and redesigned. Acoustic application notes [60, 61] are recommended. A recent work on a similar device that is used for listening to vascular sounds addresses coupling geometry and material for MEMS microphone systems [62, 63]. Their device uses a 3D printed shell structure around an air coupled microphone. A diagram of the air coupler structure is depicted in Figure 3.9. Any further design should consider air coupling dimensions by either analytically solving pressure equations [59] or doing a finite element analysis [64].

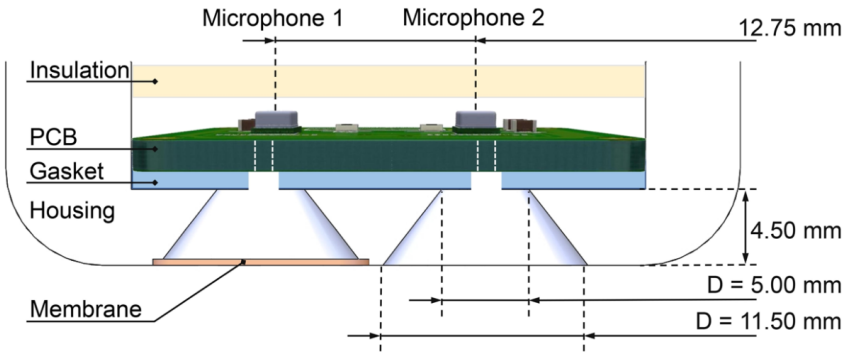

Figure 3.9. An air coupler geometry for MEMS microphones with dimensions, adapted from [62].

3.1.4. Gain Stage

Most of the electronic respiratory data acquisition systems employ a discrete instrumentation amplifier block after sensing with a microphone. Low power amplifiers are present in literature both in switched capacitor [65, 66] or continuous form [67, 68]. Sensitive MEMS microphones and a proper acoustic design could alleviate high gain requirements. An alternative of a 4-bit variable gain amplifier with track and hold is realized [69] as an example. The schematic of the switched capacitor track and hold amplifier is in Figure 3.10. A preliminary transient simulation of the gain stage is shown in Figure 3.10 where gain is -4V/V. A 4-bit digitally adjustable gain stage is implemented by using variable capacitors instead of using a single C_1 in Figure 3.10. A transient simulation of digital gain selection can be seen in Figure 3.12.

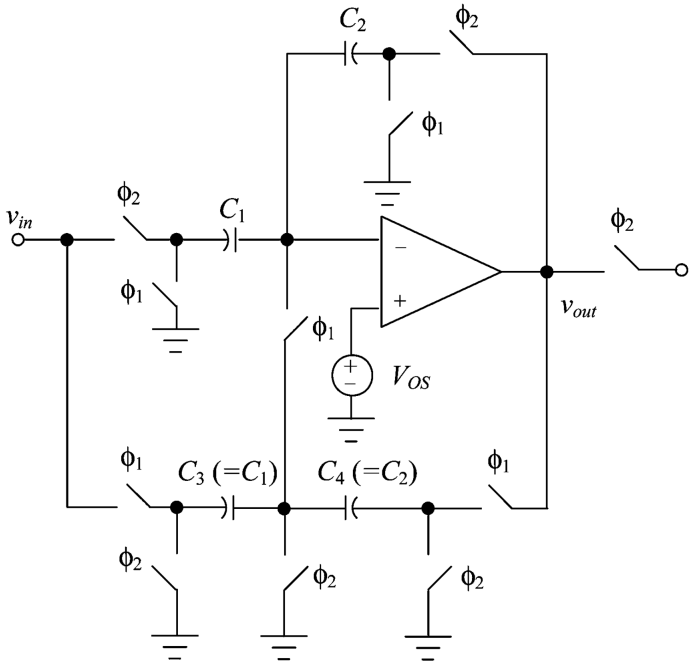

Figure 3.10. Schematic of switched capacitor track and hold amplifier, modified from [69].

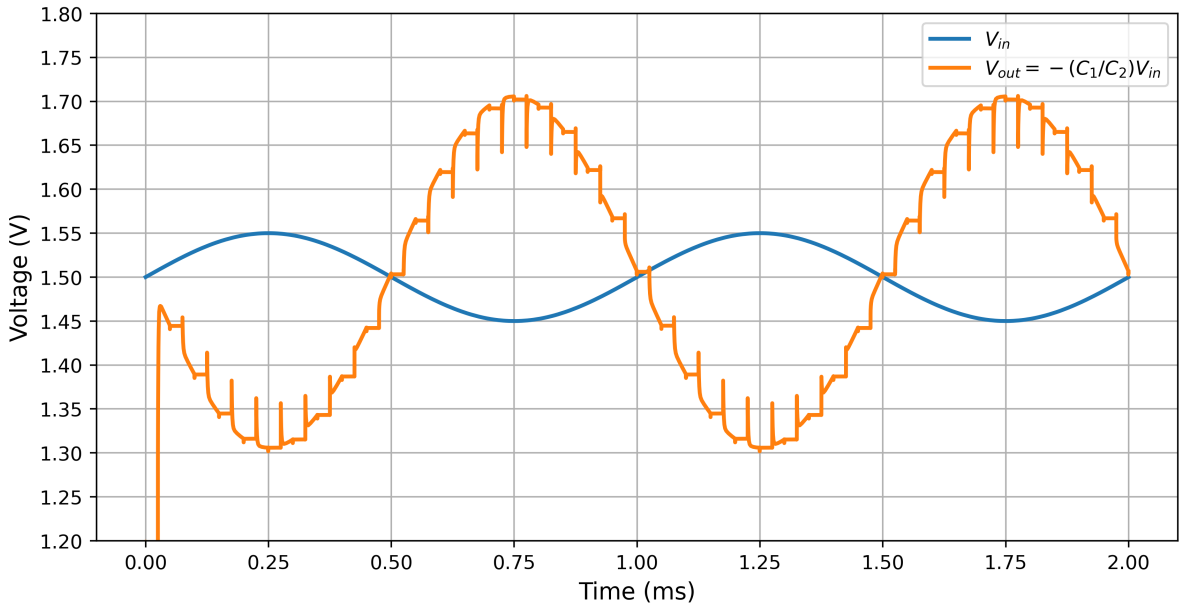

Figure 3.11. Transient response simulation of the switched capacitor gain amplifier where capacitor ratios are four.

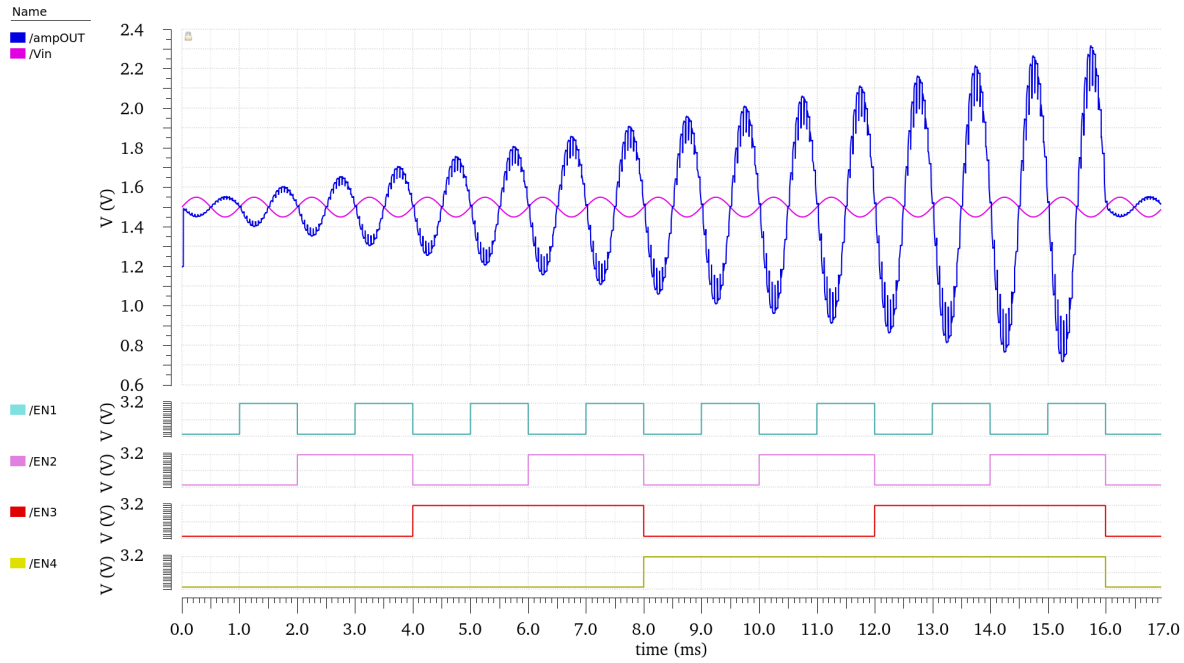

Figure 3.12. Digital gain selection simulation of the switched capacitor gain amplifier with multiple capacitors.

3.2. Filters

A filter is an electronic block that allows signal attenuation based on the frequency of the signal. Based on frequency response of the block, we can form a low pass, high pass, band pass and band reject filters. In an ideal case, filters should have a rectangular block-like response as seen in the low pass example of Figure 3.13. However, implementation of a structure with circuit elements yields different results from an ideal case. Using the previous example in Figure 3.13, a set of analog filters that approximates the given low pass response is shown including Figure 3.14. Note that an Elliptic or Chebyshev filter has a better magnitude response in terms of roll off than the same order Butterworth filter. However, a Butterworth filter has a maximally flat magnitude response in the pass band region. Having a flat passband on a low pass filter of a respiratory acquisition system is one of the recommended features of such systems according to Computerized Respiratory Sound Analysis (CORSA) guidelines [21]. In the high pass filter, a filter with an approximately linear phase response is recommended since filters with nonlinear phase response are likely to distort wave characteristics of adventitious respiratory sounds such as crackles and wheezes [17].

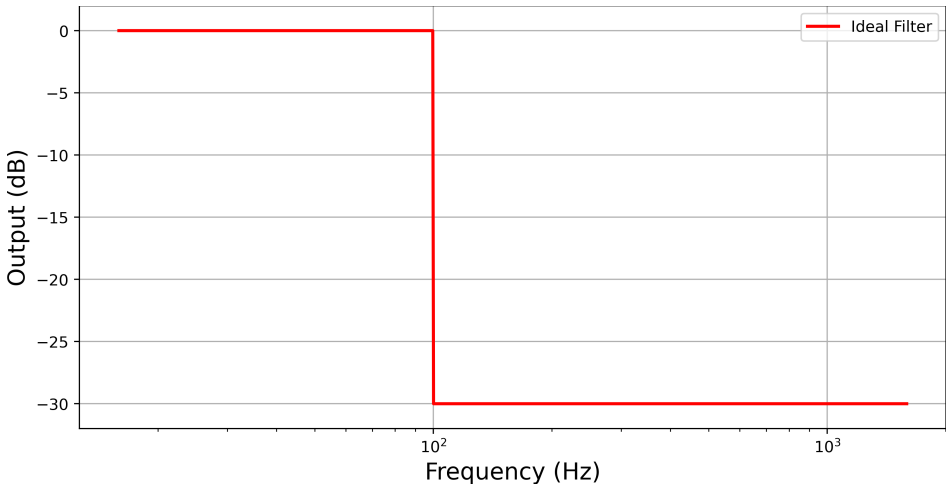

Figure 3.13. An example of an ideal low pass rectangular filter response with a cut off frequency of 100 Hz.

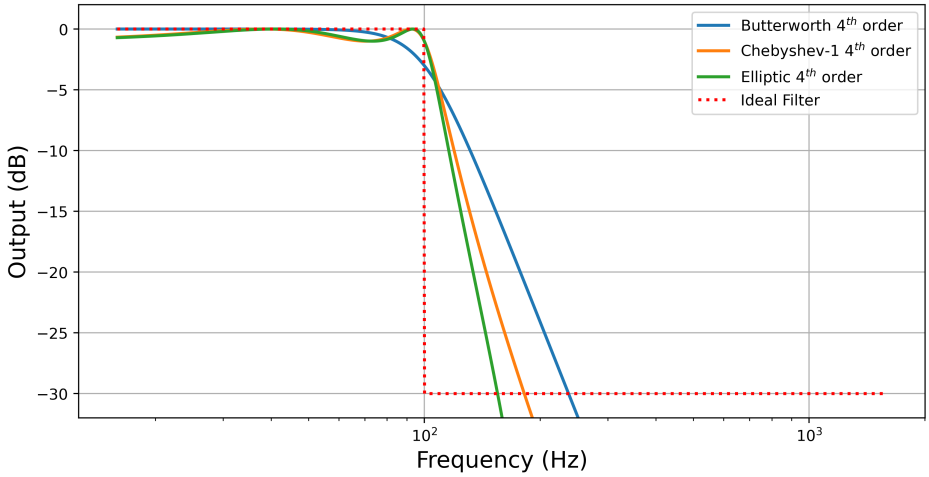

Figure 3.14. Examples of different low pass filter responses with a cut off frequency of 100 Hz.

Infinite impulse response filters can be represented in s domain. A generic transfer function for a first order general filter structure in s domain is expressed as

$$\mathbf{H}_1(s) = \frac{b_0 s + b_1}{a_0 s + a_1} \tag{3.1}$$

where $\mathbf{H_1}(s)$ is the generic first order s-domain transfer function, b_0 and b_1 are coefficients for the zero and a_0 and a_1 are coefficients for the pole in s domain, respectively. A generic transfer function for a second order general filter structure in s domain is expressed as

$$\mathbf{H}_2(s) = \frac{b_0 s^2 + b_1 s + b_2}{a_0 s^2 + a_1 s + a_2} \tag{3.2}$$

where $\mathbf{H_2}(s)$ is the generic second order s-domain transfer function, b_0, b_1 and b_2 are coefficients for zeros and a_0, a_1 and a_2 are coefficients for poles in s domain, respectively. Any analog filter block that has higher order can be constructed with cascading first and second order blocks, multiplication of first and second order s domain equations. A designer can either use extensively documented filter tables [70] or use freely available software to obtain cascaded second order blocks in s domain [71, 72]. In this thesis SciPy library of Python is used to obtain second order responses of desired analog filters of Butterworth and Bessel forms [73].

3.2.1. Design Procedure

Design of Butterworth low pass filters and Bessel high pass switched capacitor filters with multiple second order section blocks will be explained in this section. Switched capacitor circuits and integrators will be analyzed and an analysis of second order switched capacitor filters will be done by the help of analog active RC filter prototypes. Calculated unit capacitor ratio values for desired filters will be tabulated.

3.2.2. Switched Capacitor

A switched capacitor is a sampled device that can control charge transfer from a resistor [74]. A configuration as seen in Figure 3.15 is a resistor that is dependent on the sampling frequency of the non overlapping clock signals and the capacitor value.

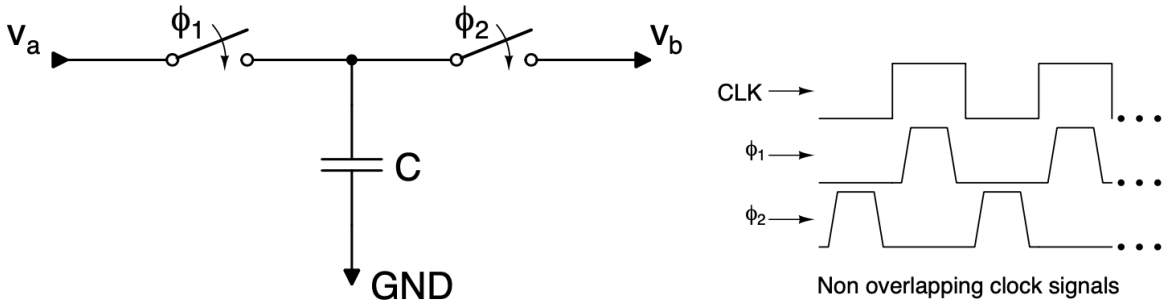

Figure 3.15. Switched capacitor as a resistor between v_a and v_b nodes under ϕ_1 and ϕ_2 clock cycles.

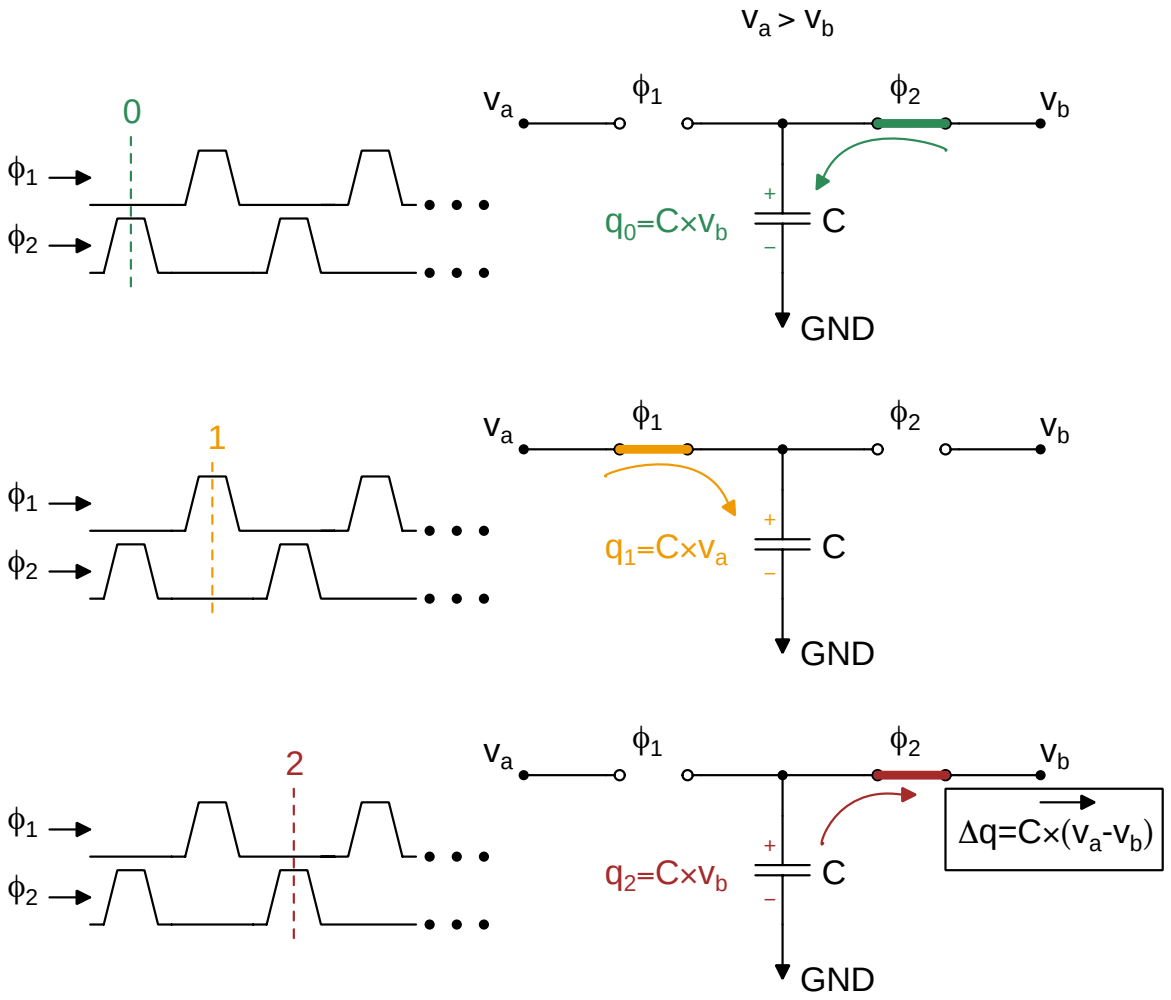

Figure 3.16. Switched capacitor charge distribution between v_a and v_b nodes under one clock cycle period.

Let's analyze the circuit in Figure 3.16 under the assumption that v_a and v_b are slowly varying signals with frequencies much smaller than the switch frequency, with capacitors time constant is much smaller than the switching period and $v_a > v_b$. We start with the time instance where only the ϕ_2 switch is closed (0). Capacitor will charge up to v_b voltage and the total charge across capacitor C is $q_0 = C \times v_b$. After half of the clock cycle where only the ϕ_1 switch is closed (1), capacitor C, holding a charge of q_0 from the previous cycle, will be charged to a larger value of $q_1 = C \times v_b$ since we have assumed $v_a > v_b$. In the next cycle (2), only the ϕ_2 switch is closed again. Voltage across the capacitor is v_b but the capacitor holds a larger charge of q_1.

Capacitor will discharge the excess part and charge difference of Δq=C $\times$ (v_a-v_b) will flow to the v_b terminal under a clock period of the switches. If we define the clock period of the switches as T, there is a net charge transfer of Δq across the terminals in every period T. Then we can write an expression of a discrete current between v_a and v_b terminals as

$$I = \frac{\Delta q}{T} = C\frac{v_a - v_b}{T} \tag{3.3}$$

where I is the discrete current that is transferred in a period T, Δq is the charge difference between nodes a and b, C is the capacitance value and v_a and v_b are node voltages of the nodes a and b, respectively. Using the frequency relationship of a clock signal $T = 1/f$, an equivalent resistance of R_{eq} can be written as

$$R_{eq} = \frac{v_a - v_b}{I} = \frac{T}{C} = \frac{1}{fC} \tag{3.4}$$

where R_{eq} is the equivalent resistance in a period T, C is the capacitance value, v_a and v_b are node voltages of the nodes a and b and f is the frequency of the switch, respectively. Note that the equivalent resistor expression at (Equation 3.4) is only true when maximum frequency component of a signal between v_a and v_b nodes are much smaller than the clock frequency of f of the switches. Also capacitor charging time constants should be much smaller than T/2 since they do require a finite time to be charged to a value with exponential approximation. If those conditions are met in a circuit, resistors can be replaced with a switched capacitor with the equivalent resistance value of $\frac{1}{fC}$. An example of such a circuit would be an integrator with an operational amplifier that is seen in Figure 3.17 with the same switching structure of Figure 3.15. Resistor of an RC integrator is replaced with a switched capacitor of C_1. Output is sampled at ϕ_1 and period of clock cycles are represented as [n] digital timesteps with respect to ϕ_1 switch clock as an example and clock cycles are long enough to ensure full charge or discharge of the capacitors during the cycles.

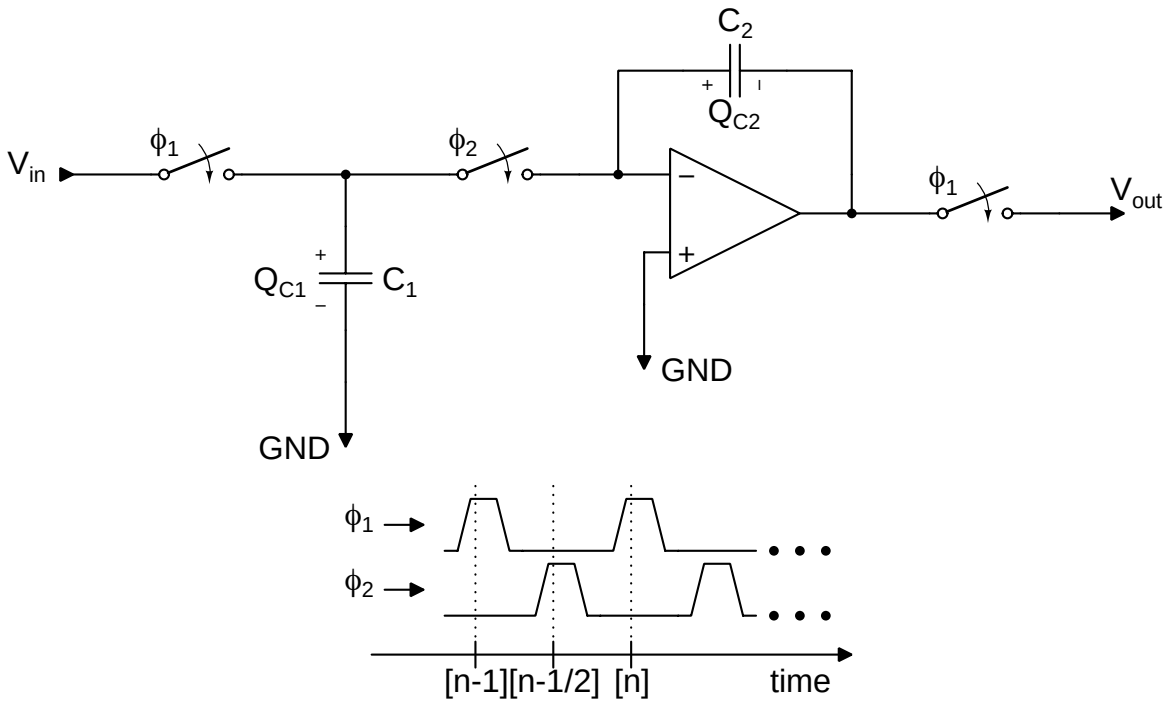

Figure 3.17. Switched capacitor integrator with parasitic sensitive capacitance configuration. Output is sampled at ϕ_1.

At [n-1] timestep, ϕ_1 switches are closed and the ϕ_2 switch is open. C_1 capacitor is charged from V_{in} to a charge value of $Q_{C1}[n-1] = C_1 V_{in}[n-1]$, and charge across C_2 capacitor at that instance is $Q_{C2}[n-1] = -C_2 V_{out}[n-1]$ since negative feedback on the ideal operational amplifier creates a virtual ground in negative terminal. At [n-1/2] timestep, ϕ_2 switch is closed and ϕ_1 switches are open. Output of the operational amplifier is disconnected from V_{out} and feedback connection of operational amplifier output via C_2 capacitor forces negative input of the amplifier to have a virtual ground. Right after the ϕ_2 switch is closed, voltage differences between C_1 capacitor terminals no longer exist since both are connected to ground. Any charge accumulated at C_1 should discharge and in the ideal case, there should be no current flowing to the amplifier negative input terminal. So all of the accumulated charge across C_1 will discharge through the feedback path of C_2 in this clock cycle. Since V_{out} is disconnected from operational amplifier output, C_2 will have a new charge value of $Q_{C2}[n-1/2] = C_1 V_{in}[n-1] - C_2 V_{out}[n-1]$ while $Q_{C1}[n-1/2] = 0$.

At [n] timestep, ϕ_1 switches are closed and the ϕ_2 switch is open again. C_1 is charged to a new value. However, C_2 has an accumulated charge from [n-1] cycle and only connection of C_2 is to the V_{out}. If we look at the charge on the C_2 at [n] it is still same as the case of [n-1/2] which is $Q_{C2}[n] = Q_{C2}[n-1/2] = C_1V_{in}[n-1] - C_2V_{out}[n-1]$. Also we can write $Q_{C2}[n]$ with an updated output voltage relation of $Q_{C2}[n] = -C_2V_{out}[n]$. Then if we equate both Q_{C2} expressions we can eliminate the charge term and we will get an input output relationship as

$$V_{out}[n] - V_{out}[n-1] = -\frac{C_1}{C_2}V_{in}[n-1] \tag{3.5}$$

where C_1 and C_2 are capacitances,V_{in} and V_{out} are input and output nodes,[n] is the discrete step value, respectively. If we take a z-transform of both sides of the (Equation 3.5),remembering that in z-transform a time delayed signal is represented as $x[n-k] \rightarrow z^{-k}X(z)$ where $k > 0$, we can write transfer function of switched capacitor parasitic sensitive integrator in z-domain as

$$\frac{V_{out}}{V_{in}}(z) = -\frac{C_1}{C_2}\frac{z^{-1}}{1-z^{-1}} \tag{3.6}$$

when output is sampled at ϕ_1 clock cycles.

Capacitor connection of the integrator shown in Figure 3.17 is prone to large parasitic capacitors from both of the switches and the top plate of the capacitor. A parasitic insensitive variant can be seen at Figure 3.18. This circuit uses two more switches to ensure parasitics at left and right terminals of C_1 are discharged to the ground. If we use the same clock cycles that are shown at Figure 3.17 we see that circuit behaves nearly the same except C_1 charge direction is inverted at each ϕ_1 clock. So for parasitic insensitive case in Figure 3.18, (Equation 3.5) changes as

$$V_{out}[n] - V_{out}[n-1] = \frac{C_1}{C_2}V_{in}[n-1] \tag{3.7}$$

where C_1 and C_2 are capacitances,V_{in} and V_{out} are input and output nodes,[n] is the discrete step value, respectively. Then subsequent z-transform leads to a value as

$$\frac{V_{out}}{V_{in}}(z) = \frac{C_1}{C_2}\frac{z^{-1}}{1-z^{-1}} \tag{3.8}$$

when output is sampled at ϕ_2 clock cycles. This output leads to a non inverting integrator.

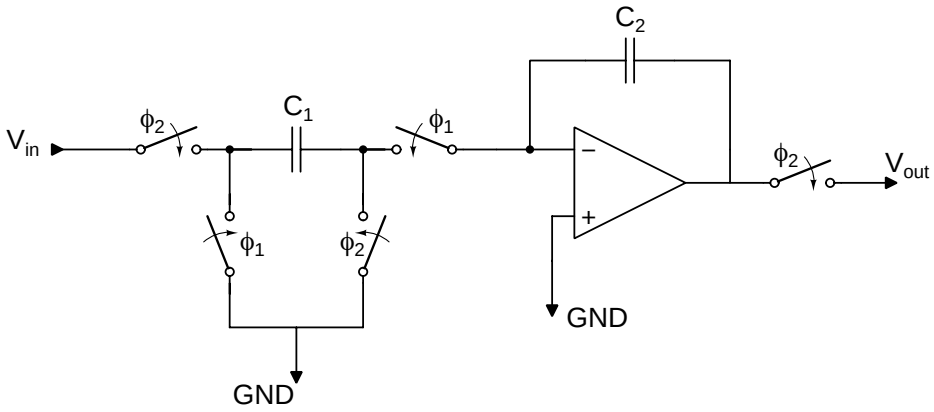

Figure 3.18. Switched capacitor integrator with parasitic insensitive capacitance configuration. Output is sampled at ϕ_2.

Another variant with parasitic insensitive switches can be seen in Figure 3.19. Since output and left and right terminals of capacitor are sampled at the same time with ϕ_2, this configuration is behaviorally the same as the parasitic sensitive case at Figure 3.17 but without a delay. This delay free integrator has a transfer function value that is expressed as

$$\frac{V_{out}}{V_{in}}(z) = -\frac{C_1}{C_2}\frac{1}{1-z^{-1}} \tag{3.9}$$

when output is sampled at ϕ_2 clock cycles. This output leads to a delay free inverting integrator.

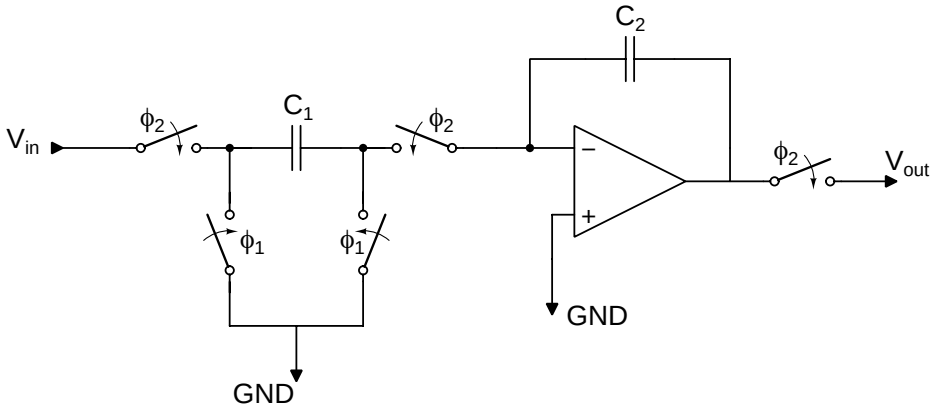

Figure 3.19. Switched capacitor delay free integrator with parasitic insensitive capacitance configuration where capacitor is discharged at ϕ_1 cycles. Output is sampled at ϕ_2.

3.2.3. Second Order Filter Prototypes

A general second order filter response is $\mathbf{H}(s) = \frac{b_0 s^2 + b_1 s + b_2}{a_0 s^2 + a_1 s + a_2}$ where b_0, b_1 and b_2 are coefficients for zeros and a_0, a_1 and a_2 are coefficients for poles in s domain, respectively. If we rearrange that equation as

$$\mathbf{H}(s) = \frac{V_{out}(s)}{V_{in}(s)} = -\frac{K_2 s^2 + K_1 s + K_0}{s^2 + \frac{\omega_0}{Q} s + \omega_0^2} \tag{3.10}$$

where K_0, K_1 and K_2 are coefficients of zeros, ω_0 is the pole frequency and Q is the pole Q factor. We define poles as $s_p = \sigma_p \pm j\omega_p$ as in the Figure 3.20, where $\omega_0 \equiv |s_p| = \sqrt{\sigma_p^2 + \omega_p^2}$ and $Q \equiv \frac{|s_p|}{2|\sigma_p|} = \frac{1}{2}\sqrt{\frac{\sigma_p^2 + \omega_p^2}{\sigma_p^2}}$.

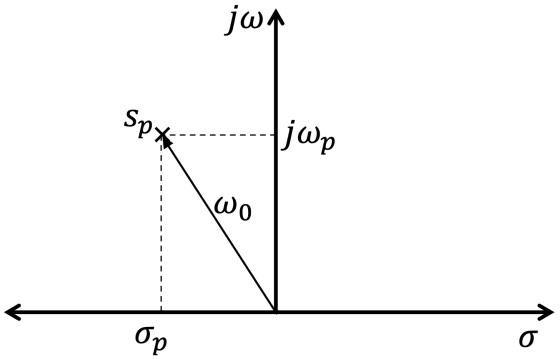

Figure 3.20. One of the complex pole in the s-plane.

To obtain signal flow graph of the second order system of (Equation 3.10), we can rewrite (Equation 3.10) as

$$s^2 V_{out}(s) = -(K_2 s^2 + K_1 s + K_0) V_{in}(s) - (\frac{\omega_0}{Q} s + \omega_0^2) V_{out}(s) \tag{3.11}$$

where K_0, K_1 and K_2 are coefficients of zeros, ω_0 is the pole frequency and Q is the pole Q factor. If we arrange the terms algebraically, we would obtain an expression as

$$V_{out}(s) = -\frac{1}{s}((K_2 s + K_1) s V_{in}(s) + \frac{\omega_0}{Q} V_{out}(s) - \omega_0 V_1(s)) \tag{3.12}$$

where $V_1(s) = -\frac{1}{s}(\frac{K_0}{\omega_0} V_{in}(s) + \omega_0 V_{out}(s))$. Note that V_1 can be chosen differently without a change in the definition [75]. Signal flow graph of the (Equation 3.12) can be seen in Figure 3.21.

An active RC implementation of Figure 3.21 can be done by placing continuous inverting integrators with a unit capacitor when there is a block of [-1/s], putting a capacitor on terms that are multiplied with [s] and putting a resistor value of reciprocals of constant terms as seen in the Figure 3.22.

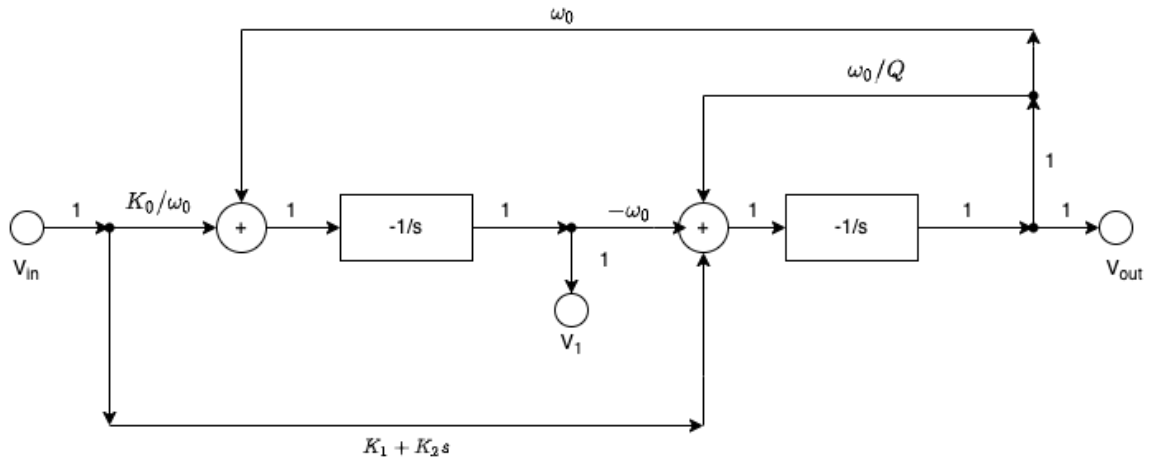

Figure 3.21. Signal flow graph of the second order filter response, modified from [75].

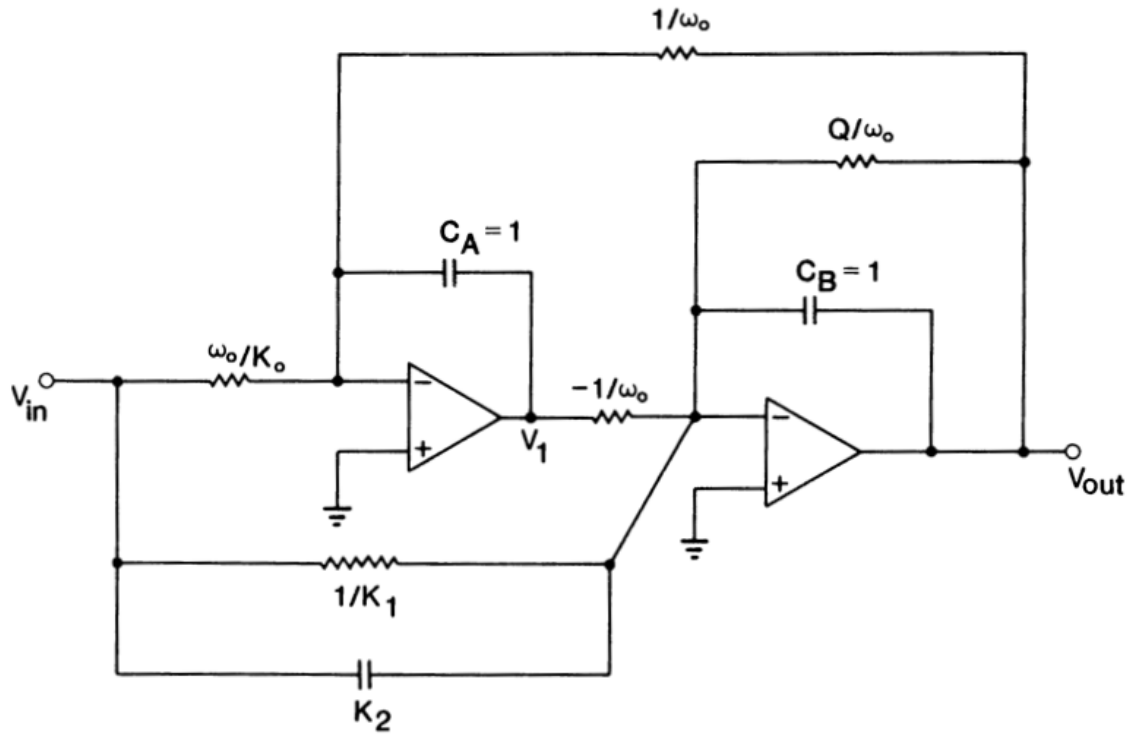

Figure 3.22. Active RC implementation of the signal flow graph of Figure 3.21, adapted from [75].

Note that a negative resistance of $-1/\omega_0$ is present in Figure 3.22 which is not possible with passive elements. However, this active RC implementation can be translated to a switched capacitor version by substituting

- Negative resistor → Parasitic free switched capacitor integrator (Figure 3.18)
- Positive resistor → Delay free switched capacitor integrator (Figure 3.19)
- Capacitor → Capacitor

After substitution, we can realize the circuit seen in Figure 3.23 [75] by using a V_{ref} value as a virtual ground. Note that some of the switches are shared to reduce components.

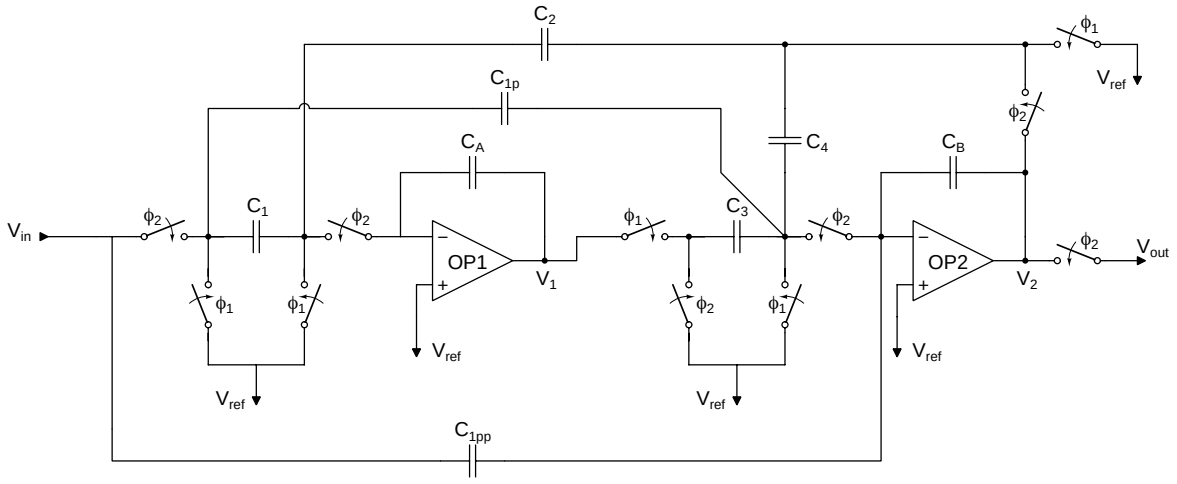

Figure 3.23. Second order low Q switched capacitor filter schematic with two operational amplifiers and non overlapping switches, modified from [75].

Component values for the circuit in Figure 3.23 where switches are sampled with a period of T can be approximated as $C_1 \rightarrow TK_0/\omega_0,\ C_2 \rightarrow \omega_0 T,\ C_3 \rightarrow \omega_0 T,\ C_4 \rightarrow \omega_0 T/Q,\ C_{1p} \rightarrow K_1 T,\ C_{1pp} \rightarrow K_2$. This approximation is true only when $|w_0 T| << 1$ such that sampling frequency is much larger than filter frequency ranges. To alleviate approximation, an exact analysis of the switched capacitor circuit can be done by constructing a z-transform signal flow graph.

By using a capacitor, a non inverting switched capacitor integrator and a delay free switched capacitor integrator we can form a signal flow graph example as seen in Figure 3.24. Note that C_1 and C_4 capacitors in Figure 3.24 are not switched capacitors. Transfer function of a non switched capacitor and an integrator is $H_1(z) = -\frac{C_1}{C_4}$ thus first branch is multiplied with $(1-z^{-1})$ term to make transfer function correct. Output node can be expressed as sum of the three input voltages with their coefficients on the path of signal flow chart as

$$V_{out}(z) = \frac{-C_1}{C_4}V_1(z) + \frac{C_2 z^{-1}}{1-z^{-1}}V_2(z) + \frac{-C_3}{1-z^{-1}}V_3(z) \tag{3.13}$$

where $V_1(z), V_2(z)$ and $V_3(z)$ are z transforms of the input voltages V_1, V_2 and V_3 and C_1, C_2, C_3 and C_4 are capacitors in Figure 3.24 with the switches of ϕ_1 and ϕ_2.

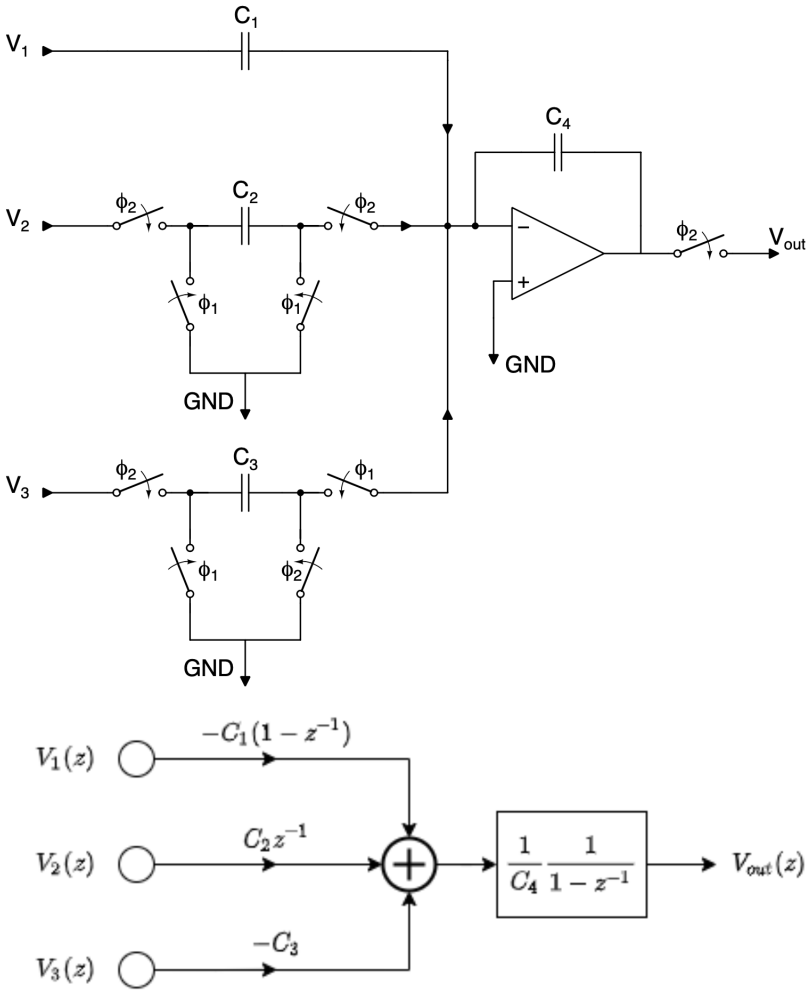

Figure 3.24. Signal flow chart of a switched capacitor integrator circuit with different inputs and their z-transforms.

If we change switched capacitors that are shown in Figure 3.23 to a signal flow chart, we will get a flow graph seen in Figure 3.25.

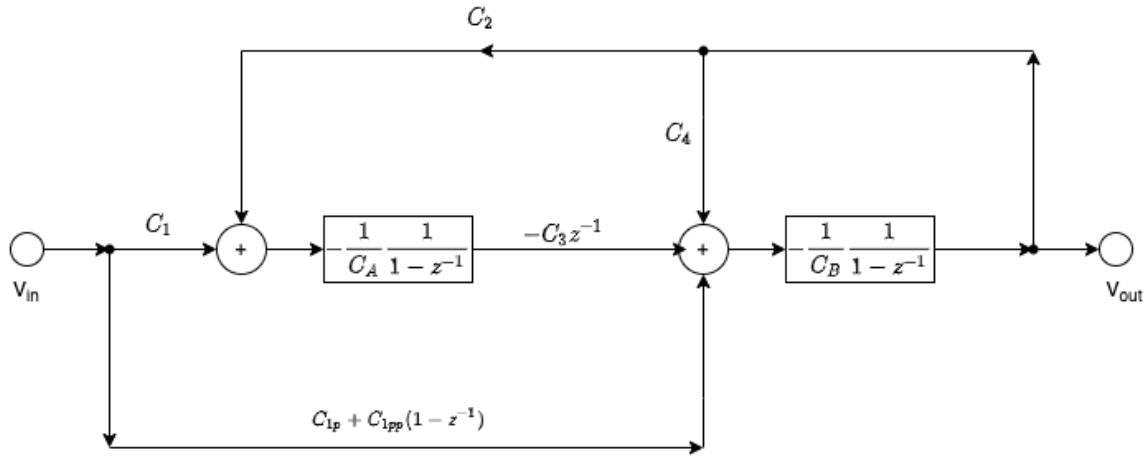

Figure 3.25. Signal flow graph for exact analysis of the switched capacitor biquadratic filter prototype, adapted from [75].

Transfer function for a switched capacitor second order filter in the z domain is expressed as

$$H(z) = \frac{V_{out}(z)}{V_{in}(z)} = -\frac{(C_{1p} + C_{1pp})z^2 + (C_1C_3 - C_{1p} - 2C_{1pp})z + C_{1pp}}{(1 + C_4)z^2 + (C_2C_3 - C_4 - 2)z + 1} \tag{3.14}$$

where $C_1,\ C_{1p},\ C_{1pp},\ C_2,\ C_3$ and C_4 are capacitors that are used in Figure 3.23.

Any second order filter structure in the z domain that satisfies (Equation 3.14) can be realized by using Figure 3.23. A general z domain transfer function is expressed as $H_g(z) = -\frac{a_2z^2+a_1z+a_0}{b_2z^2+b_1z+1}$. If we use this general z domain transfer function in (Equation 3.14) under the assumption $C_2 = C_3$ to minimize spread, we will obtain capacitor values that are represented in Table 3.2 for the cases where $Q < 3$.

Table 3.2. Exact capacitor values for a second order filter with low Q.

Capacitor name	**Generalized values**
C_A	1
C_B	1
C_{1pp}	a_0
C_{1p}	$a_2 - a_0$
C_1	$(a_2 + a_1 + a_0)/\sqrt{b_1 + b_2 + 1}$
C_2	$\sqrt{b_1 + b_2 + 1}$
C_3	$\sqrt{b_1 + b_2 + 1}$
C_4	$b_2 - 1$

Table 3.2 gives exact capacitor values for a second order filter in the z domain. This circuit can realize stable filters where poles are within the unit circle in z domain. A limitation of this filter is that capacitor ratios of this configuration are better suited for low Q ($Q < 3$) poles. A variant for high Q ($Q \geq 3$) poles can be constructed as in Figure 3.26 with the equation expressed as

$$H_2(z) = \frac{V_{out}(z)}{V_{in}(z)} = -\frac{C_{1pp}z^2 + (C_1C_3 + C_{1p}C_3 - 2C_{1pp})z + (C_{1pp} - C_{1p}C_3)}{z^2 + (C_2C_3 + C_4 - 2)z + (1 - C_3C_4)} \tag{3.15}$$

where $C_1,\ C_{1p},\ C_{1pp},\ C_2,\ C_3$ and C_4 are capacitors that are used in Figure 3.26. The capacitor values for high Q cases are represented in Table 3.2 for the cases where $Q \geq 3$ under the assumption $C_2 = C_3$ to minimize spread.

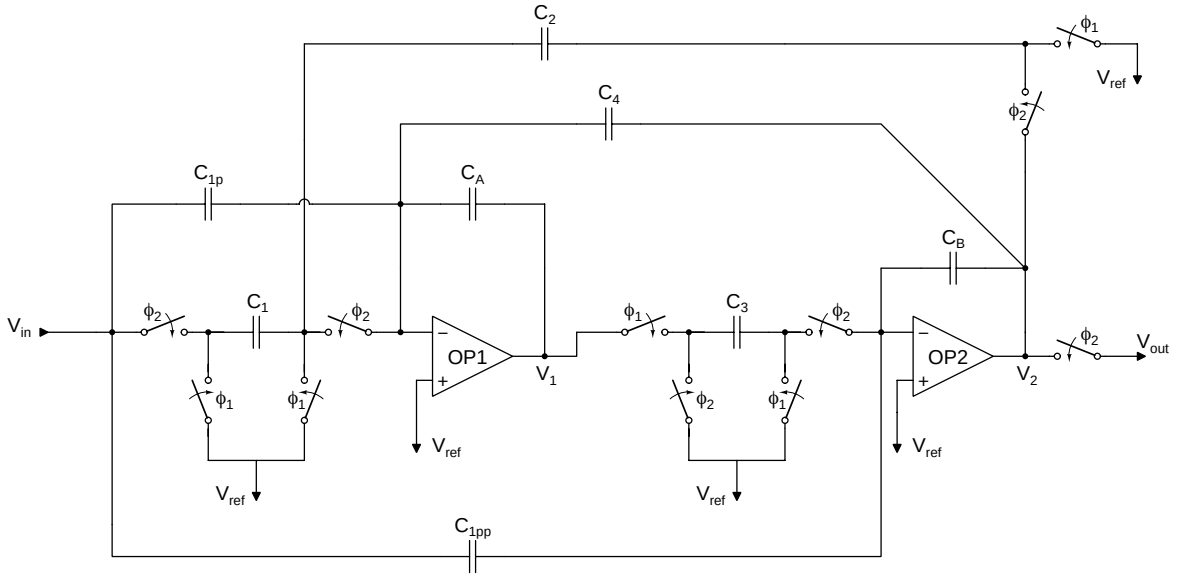

Figure 3.26. Second order high Q switched capacitor filter schematic with two operational amplifiers and non overlapping switches, modified from [75].

Table 3.3. Exact capacitor values for a second order filter with high Q.

Capacitor name	**Generalized values**
C_A	1
C_B	1
C_{1pp}	a_2/b_2
C_{1p}	$(a_2 - a_0)/(\sqrt{(b_1 + b_2 + 1)b_2})$
C_1	$(a_2 + a_1 + a_0)/(\sqrt{(b_1 + b_2 + 1)b_2})$
C_2	$\sqrt{(b_1 + b_2 + 1)/b_2}$
C_3	$\sqrt{(b_1 + b_2 + 1)/b_2}$
C_4	$(1 - 1/b_2)/(\sqrt{(b_1 + b_2 + 1)/b_2})$

Both low Q and high Q second order transfer functions in z domain are possible by substituting capacitance values Table 3.2 and Table 3.3 respectively. In the next section, an operational amplifier, a switch realization is discussed and details of capacitance scaling is explained.

4. FILTER IMPLEMENTATION

4.1. Operational Amplifier

A large gain rail to rail input output folded cascode operational amplifier is designed to have a good approximation of the ideal operational amplifier. Also a high slew rate is required for filtering applications with switched capacitors.

4.1.1. Design Parameters

Gain bandwidth product of the operational amplifier should be at least 5 times large from the sampling clock frequency to be used in switched capacitor filters [75]. In this design, switching frequency of the swithces are chosen as 20 kHz so a minimum of 100 kHz gain bandwidth product should be attained. Also slew rate of the operational amplifier should be large enough to account for the mid point to rail swing on a switch cycle.

A folded cascode operational amplifier with NMOS and PMOS differential input pairs are designed. Schematic of input and output stages can be seen in Figure 4.1 and output bias voltage stages can be seen in Figure 4.2.

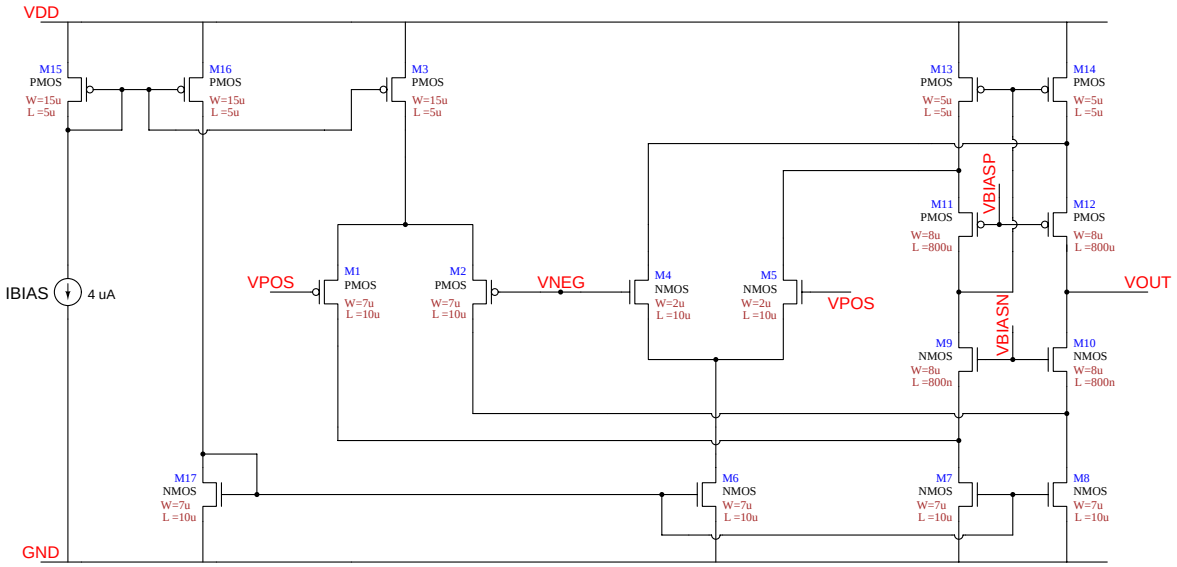

Figure 4.1. Schematic view of the folded cascode rail to rail operational amplifier with external bias voltages.

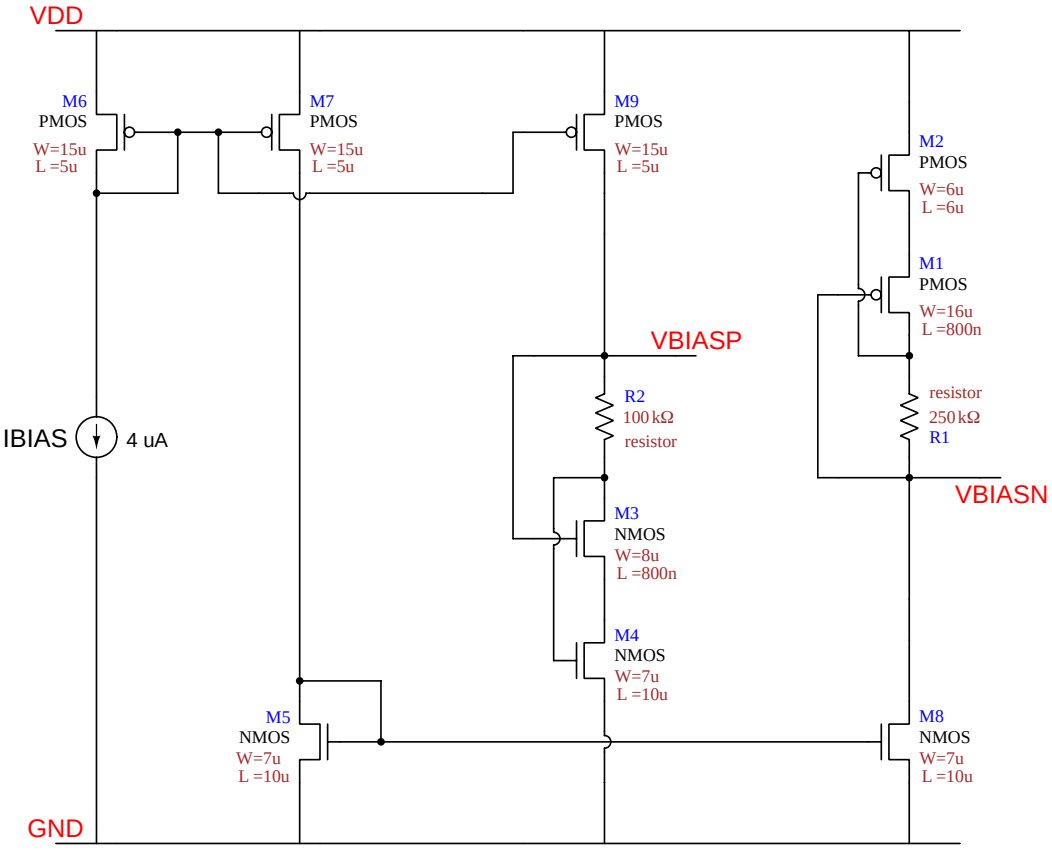

Figure 4.2. Schematic view of the output bias circuit.

4.1.2. Layout Considerations

Input PMOS and NMOS differential stage transistors need to be well matched. To improve matching of those, transistors were split into two parallel stages with half of their widths and connected in parallel with equal length gate connectors as seen in the Figure 4.3

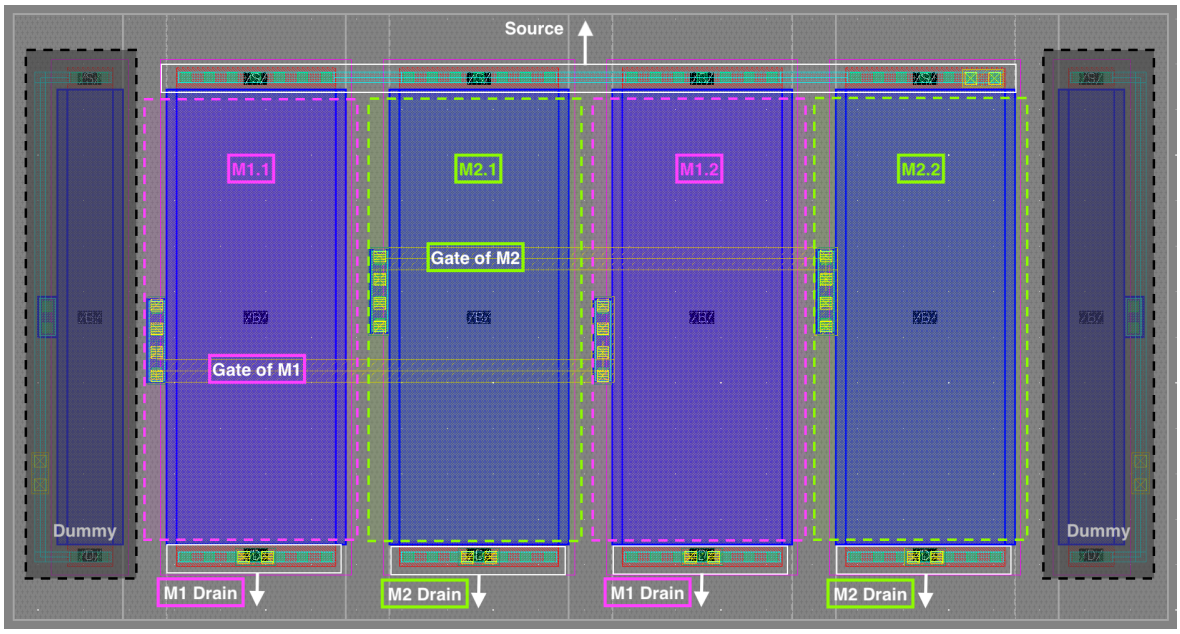

Figure 4.3. Improvement of the matching on the PMOS transistors in input differential stage, two transistors having a $\frac{W}{2}$ width are connected parallel from their gates in an alternating fashion.

An overview of the operational amplifier layout can be seen at Figure 4.4 and the bias circuit for output stage is not shown here. Input stage is rotated to fit a rectangular shape as seen in the left part. Alternating parallel NMOS and PMOS input transistors are expressed as "ABAB". On the top and bottom PMOS and NMOS current mirrors are placed with their dummy transistors. Output stage is placed at the right part of the circuit. Metal-1 connections were used mostly to connect internal units, Metal-2 lines were used for vertical interconnects and Metal-3 lines were used for horizontal interconnects and pin connections.

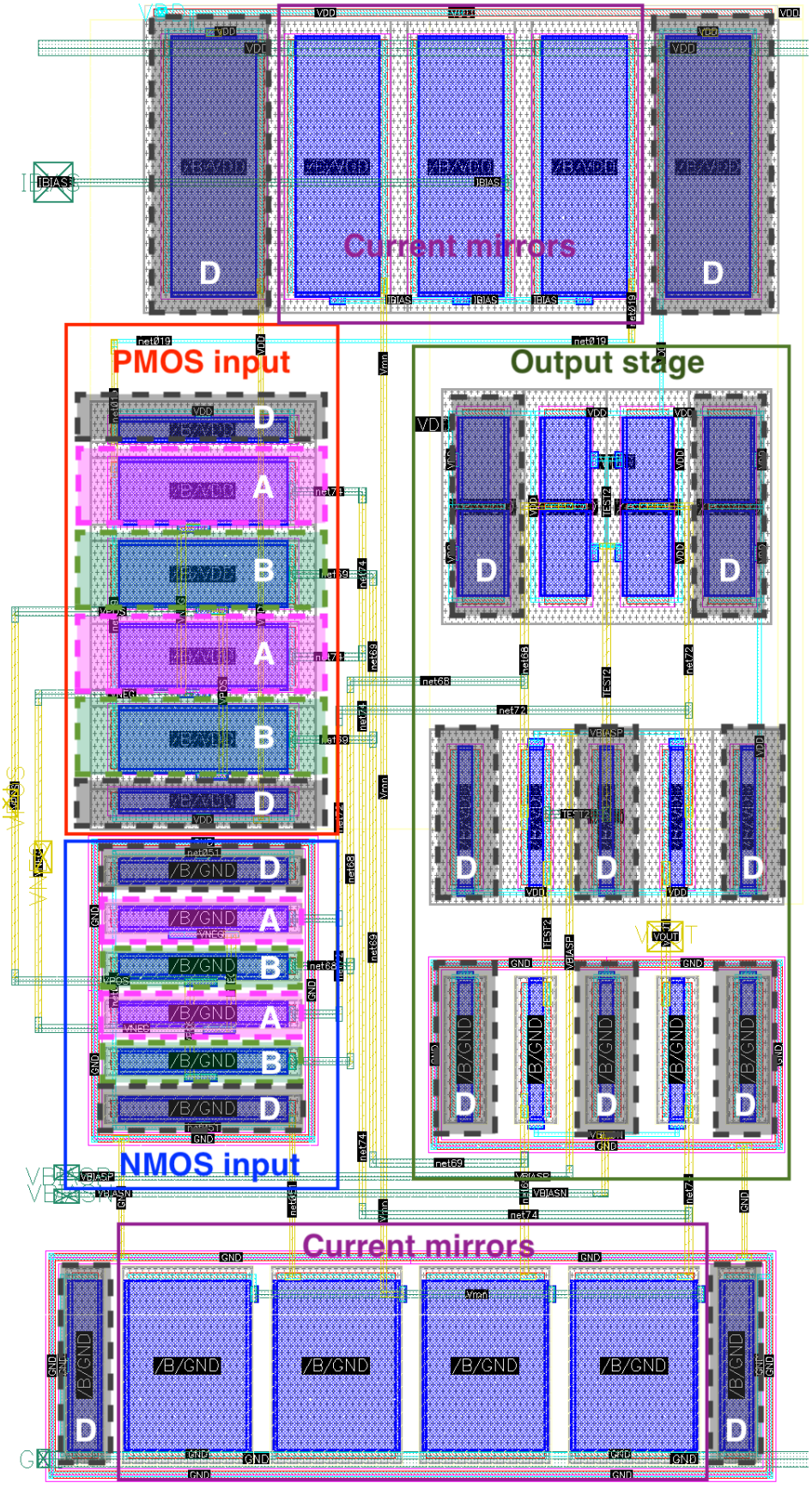

Figure 4.4. Layout of the folded cascode rail to rail OPAMP.

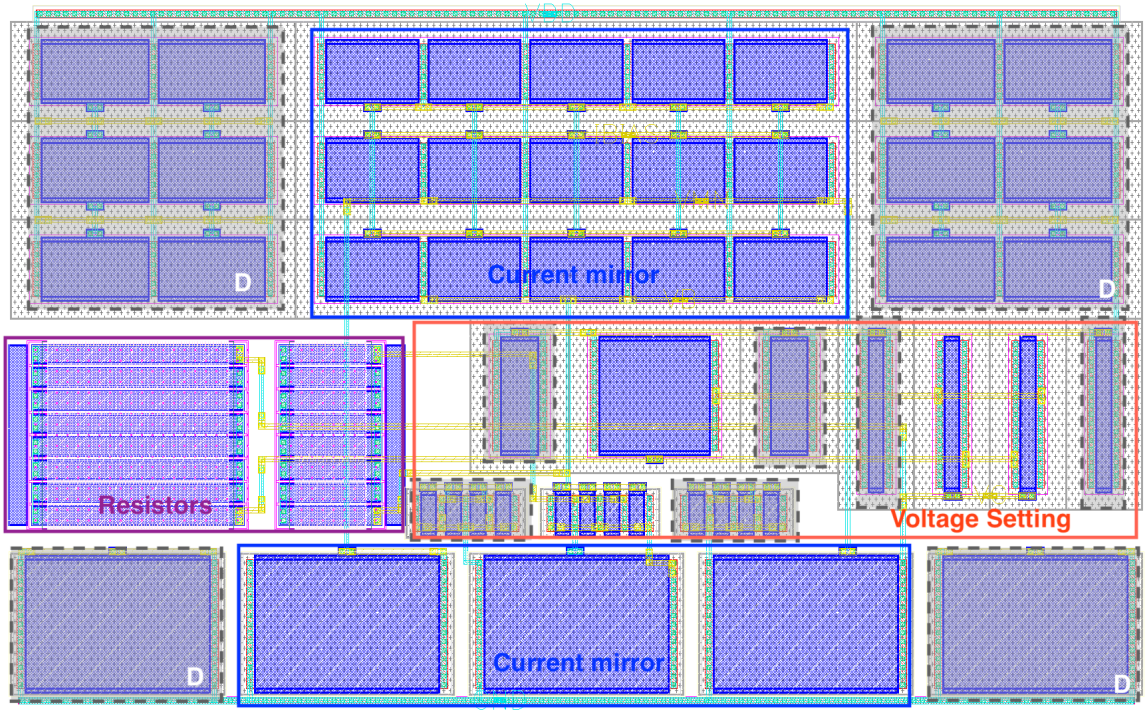

Figure 4.5. Layout of the output bias circuit.

4.1.3. AC Simulation

An AC analysis of the designed operational amplifier under different capacitive loads can be seen in Figure 4.6. DC gains and gain bandwidth products (GBW) are tabulated in Table 4.1. A high DC gain of 78 dB is observed in the schematic level and DC gain is slightly reduced to 74.5 dB after parasitic extraction of the operational amplifier layout. A gain bandwidth simulation under different DC common modes is performed to investigate performance of the operational amplifier during switching. Results can be seen in Figure 4.7 and Figure 4.8. As seen in the gain bandwidth case, higher load capacitances might compromise the margin requirements of the gain bandwidth product since they need to be larger than five times of the clock switching frequencies of switched capacitors.

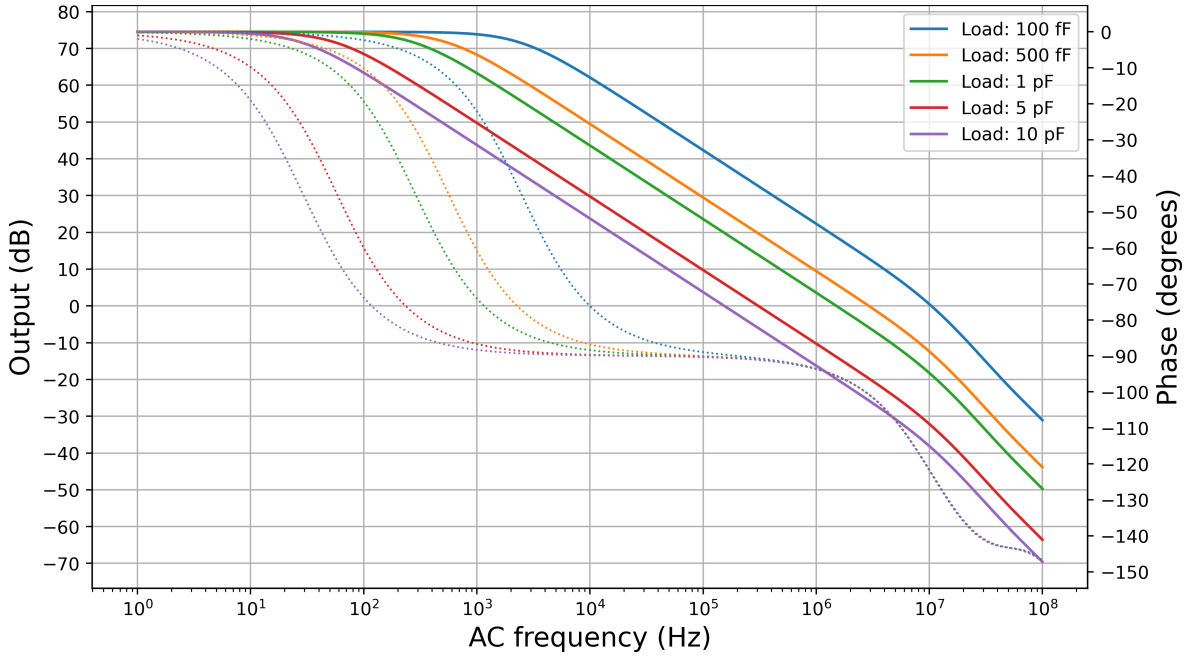

Figure 4.6. AC analysis of folded cascode rail to rail operational amplifier under capacitive loads of 100 fF, 500 fF, 1 pF, 5 pF and 10 pF.

Table 4.1. DC gain and gain bandwidth product results of operational amplifier in ideal and post layout AC simulation results in Figure 4.6.

Load Capacitance	**Ideal**		**Post Layout**	
	DC Gain (dB)	GBW	DC Gain (dB)	GBW
100 fF	78.36	10.97 MHz	74.52	10.47 MHz
500 fF	78.36	3.042 MHz	74.52	2.967 MHz
1 pF	78.36	1.563 MHz	74.52	1.533 MHz
5 pF	78.36	318.7 kHz	74.52	312.4 kHz
10 pF	78.35	159.8 kHz	74.51	156.8 kHz

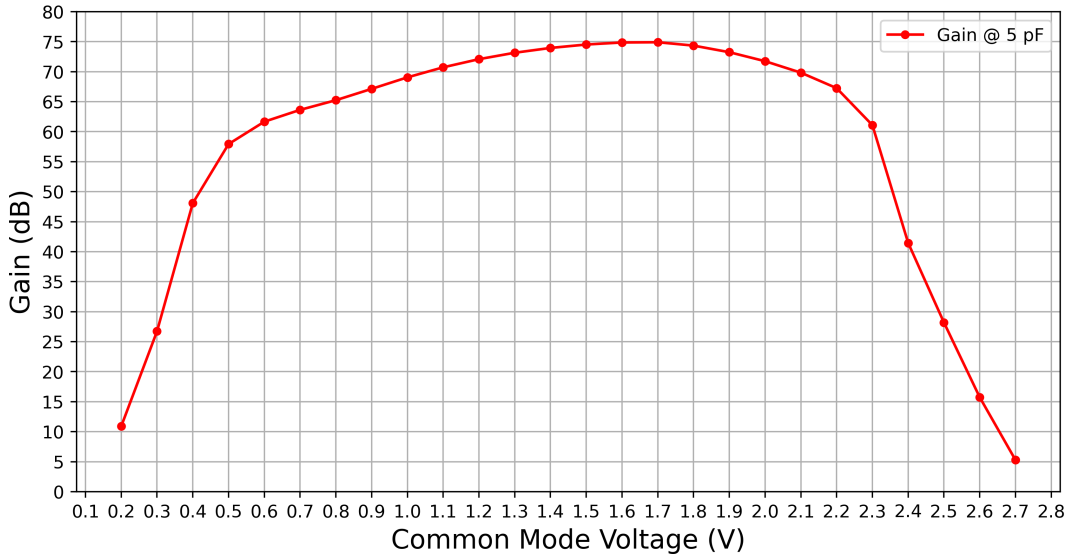

Figure 4.7. Gain of operational amplifier under different common mode DC voltages. Load capacitance is 5 pF.

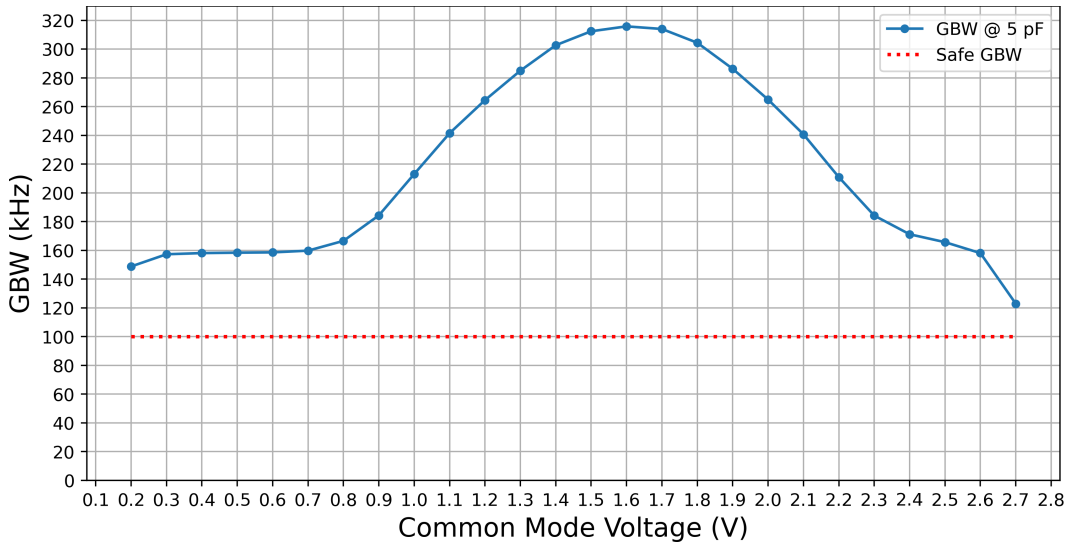

Figure 4.8. Gain of operational amplifier under different common mode DC voltages. Load capacitance is 5 pF.

4.2. Transmission Gate

Minimum length transmission gates will be used as switches to allow correct switching in rail to rail swings. In this technology, a special transistor that is tolerant for higher voltages (up to 5V) will be used. PMOS and NMOS transistors will have the same size to minimize timing differences during switching. Schematic of the transmission gate can be seen in Figure 4.9 and layout of the transmission gate can be seen in Figure 4.10.

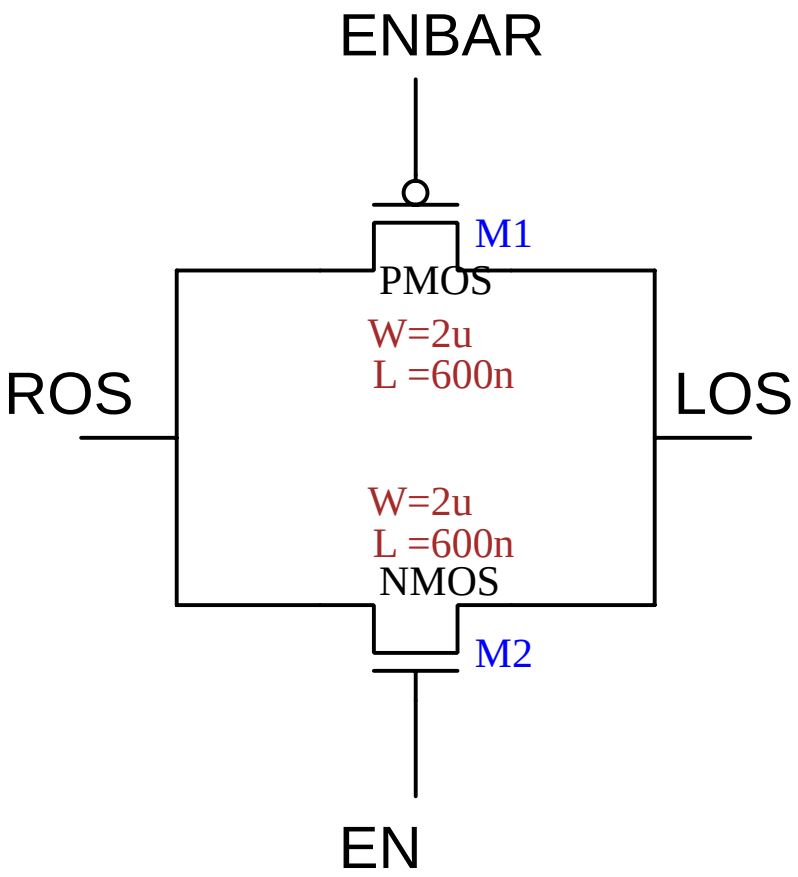

Figure 4.9. Schematic of a transmission gate with sizes.

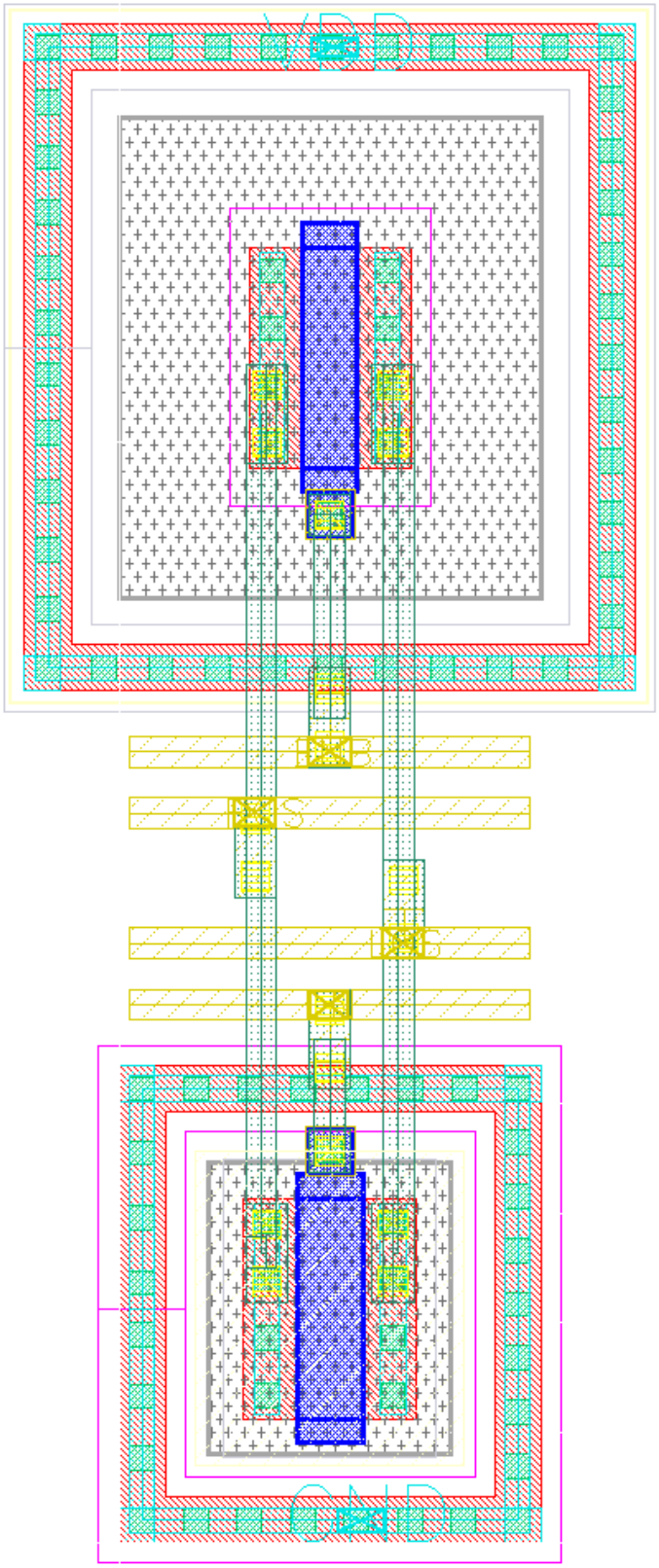

Figure 4.10. Layout of a transmission gate.

4.3. Capacitor Sizing, Scaling and Layout

4.3.1. Low Pass Filters

A sixth order Butterworth low pass filter will be designed in three sections. Ratio between cut off f_{-3db} and a clock frequency f_c will be 1/10. By using a clock frequency $f_c = 20$ kHz we can get a cut off frequency of $f_{-3db} = 2$ kHz.

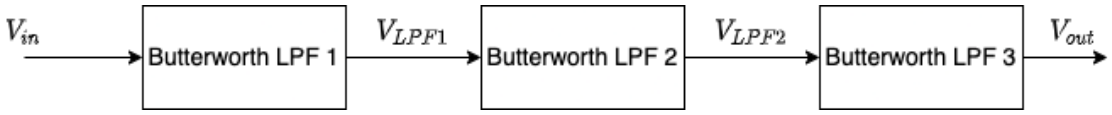

Figure 4.11. Butterworth low pass filter second order sections.

For Butterworth filters, second order cascaded filter stages can be found either by using filter tables [70] or using filter design tools [73]. A prewarping technique is applied before bilinear transformation of s domain analog filter prototypes to z domain [71]. In this example, zpk2sos function from the Python SciPy library is used to determine second order stages from pole zero locations after bilinear transformation. Function gives numerator and denominator values of z transform as $H_{zpk2sos}(z) = \frac{n_2 z^2 + n_1 z + n_0}{d_2 z^2 + d_1 z + d_0}$ where coefficients are represented as a Nx6 matrix for a filter with 2N stages. Values are tabulated in Table 4.2.

Table 4.2. Table for Butterworth low pass filter second order stages before gain scaling and normalization.

	n_2	n_1	n_0	d_2	d_1	d_0
Stage 1	3.405e-4	6.811e-4	3.405e-4	1.000e+0	-1.032e+0	2.757e-1
Stage 2	1.000e+0	2.000e+0	1.000e+0	1.000e+0	-1.143e+0	4.128e-1
Stage 3	1.000e+0	2.000e+0	1.000e+0	1.000e+0	-1.404e+0	7.359e-1

However, Python implementation of the function always returns total gain (k) constant on the numerator of the first stage as seen in Table 4.2. All of the subsequent numerators are normalized and the first stage numerator is multiplied by k. Gain of individual stages should be scaled evenly before proceeding. So, in this specific example, all of the numerators n_2, n_1, n_0 are multiplied with the cube root of the constant k. Low Q switched capacitor second order filter prototype has a form of $H_g(z) = -\frac{a_2 z^2 + a_1 z + a_0}{b_2 z^2 + b_1 z + 1}$ where denominator constant term $b_0 = 1$. To match that, d_0 term should be equal to one and by dividing every value of the matrix by d_0. Gain scaled and normalized transfer function values are presented at Table 4.3 for sixth order Butterworth low pass filter.

Table 4.3. Table for Butterworth low pass filter second order stages after gain scaling and normalization.

	n_2	n_1	n_0	d_2	d_1	d_0
Stage 1	2.533e-1	5.066e-1	2.533e-1	3.627e+0	-3.743e+0	1.000e+0
Stage 2	1.692e-1	3.383e-1	1.692e-1	2.422e+0	-2.769e+0	1.000e+0
Stage 3	9.489e-2	1.898e-1	9.489e-2	1.359e+0	-1.908e+0	1.000e+0

Then, if we use Table 3.2 to find capacitor values of the circuit in Figure 3.23, we would get the capacitor values presented in Table 4.4. Note that C_A and C_B capacitors have unit value of 1 and all of the rest are ratio values of capacitors with respect to unit value.

In second order section filter structures, a scaling of capacitors is required to equalize dynamic range of the filters. If we run simulation with the capacitance values of Table 4.4 with unit capacitor being 1 pF, we would get transfer functions shown in Figure 4.12.

Table 4.4. Table for ideal output capacitance ratios for switched capacitor second order low pass filter (LPF) sections before scaling.

Variable name	**LPF Section 1**	**LPF Section 2**	**LPF Section 3**
C_1	1.0777	0.8370	0.5655
C_2	0.9400	0.8085	0.6712
C_A	1	1	1
C_4	2.6270	1.4225	0.3589
C_3	0.9400	0.8085	0.6712
C_{1pp}	0.2533	0.1692	0.0949
C_B	1	1	1

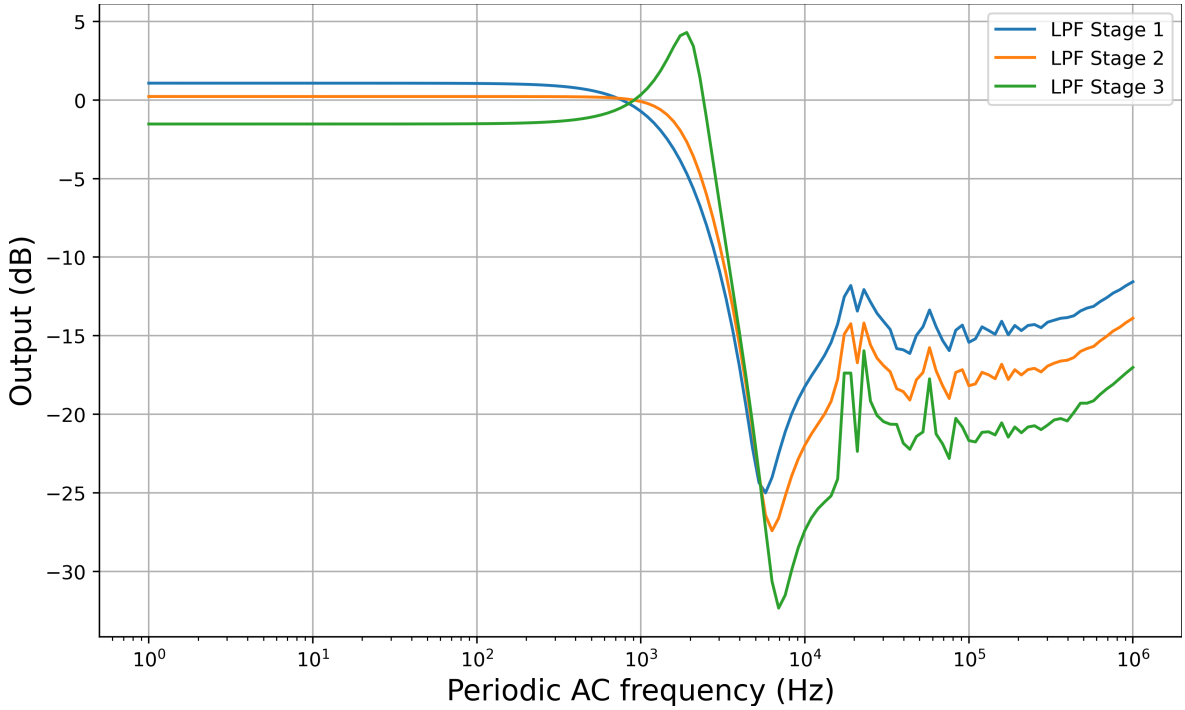

Figure 4.12. Butterworth low pass filter second order section outputs before dynamic scaling.

Scaling is done by finding the maximum of transfer function for each operational amplifier output. Then capacitor values that are connected to the outputs of each operational amplifier are multiplied by the maximum value of each operational amplifier.

Corresponding capacitors are shown in Figure 4.13, C_A and C_3 are multiplied by the maximum value of OP1 output (V_1) transfer function and C_2, C_4 and C_B are multiplied by the maximum value of OP2 output (V_2) transfer function.

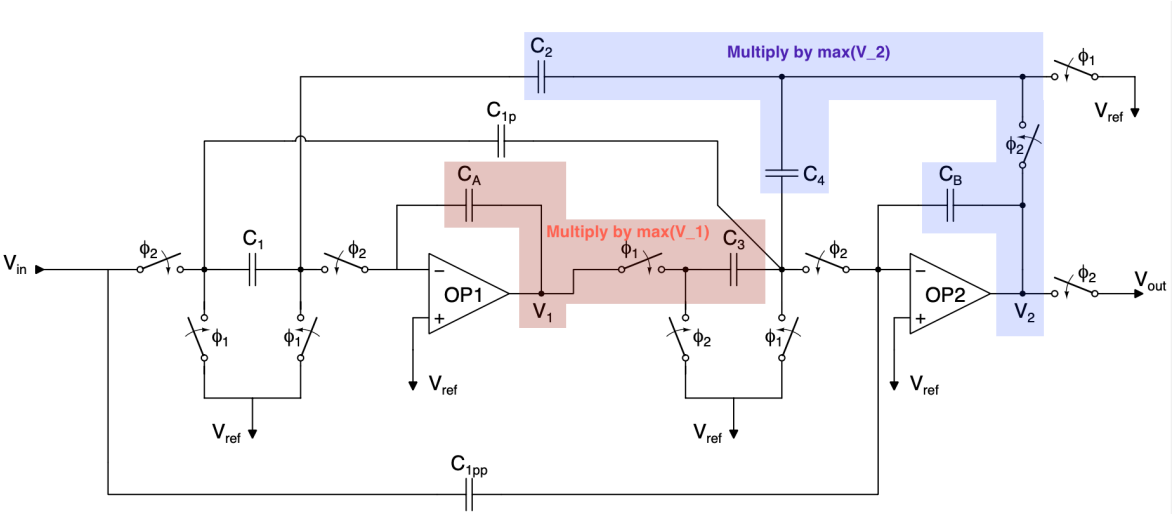

Figure 4.13. Scaled capacitors due to peaking at low Q switched capacitor prototype.

If we scale corresponding capacitors, we would get the capacitance values of Table 4.5 in the case of Butterworth low pass filters and simulation with the capacitance values of Table 4.5 with unit capacitor being 1 pF will result scaled outputs for all of the sections as shown in Figure 4.14.

Table 4.5. Table for ideal output capacitance ratios for switched capacitor second order low pass filter (LPF) sections after dynamic scaling.

Variable name	**LPF Section 1**	**LPF Section 2**	**LPF Section 3**
C_1	1.078	0.837	0.5655
C_2	1.058	0.8271	1.098
C_A	3.198	1.897	1.957
C_4	2.955	1.455	0.5872
C_3	3.006	1.534	1.314
C_{1pp}	0.2533	0.1692	0.09489
C_B	1.125	1.023	1.636

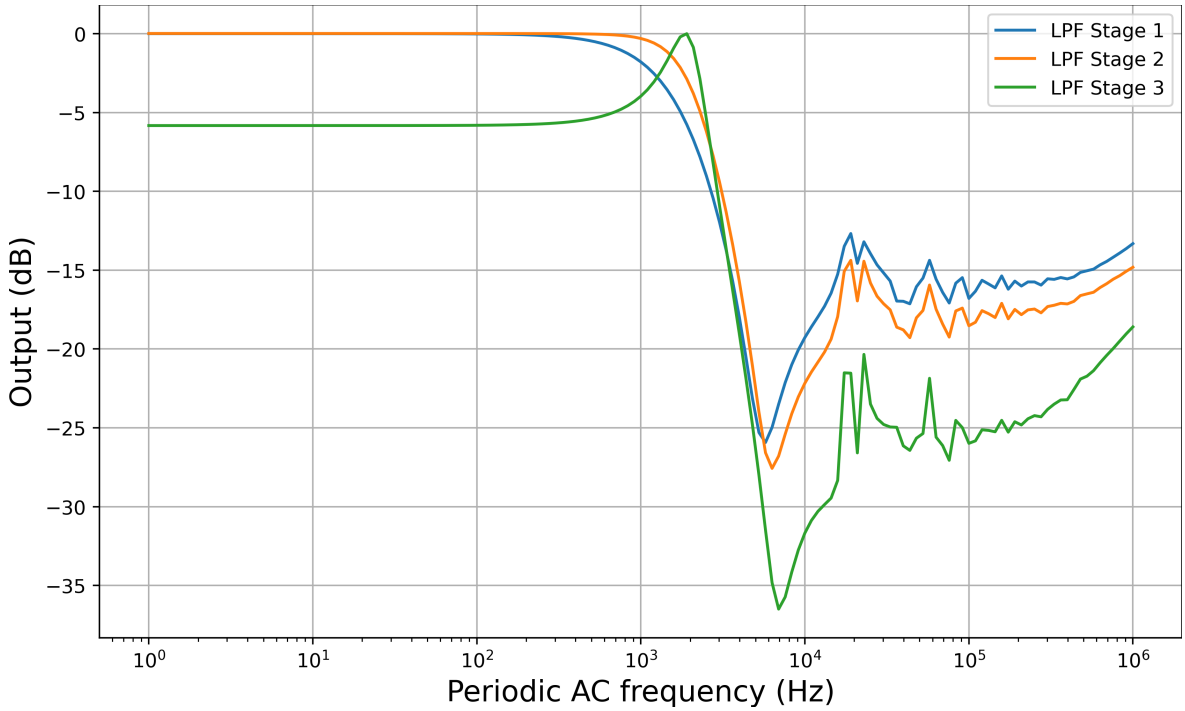

Figure 4.14. Butterworth low pass filter second order section outputs after dynamic scaling.

Layout of a non-integer capacitor ratio will have problems in matching. A good practice is to have them in unit capacitors and have an integer ratio between them. Tests are done on low pass filters as seen in Figure 4.15, Figure 4.16 and Figure 4.17 to find optimal integer ratios. The most suitable integer ratios are listed in Table 4.6. Note that maximum capacitance spread is 30 in all of the sections. If we use a unit capacitor of 100 fF, maximum capacitance would be 3 pF which is below the limit of the operational amplifier.

A partial layout of capacitors can be seen in Figure 4.18 where Metal Insulator Metal capacitors are used in between Metal-5 and Metal-6 layers. Parallel unit capacitors are connected with Metal-5 and Metal-6 lines and ports are made with Metal-4 and Metal-5.

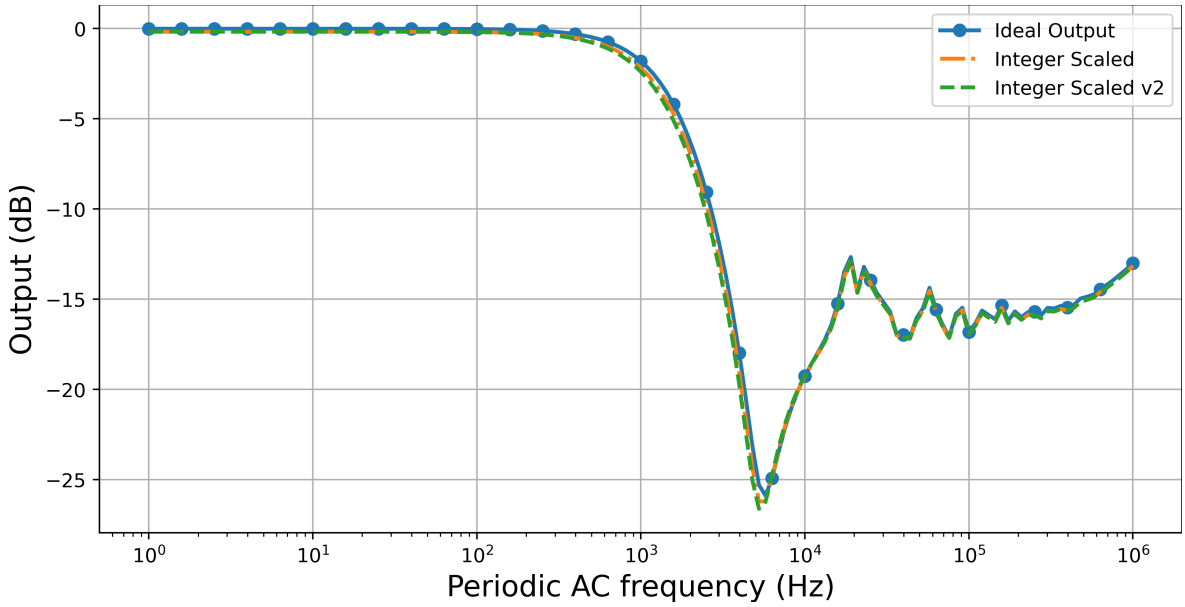

Figure 4.15. Butterworth low pass filter biquadratic sections magnitude responses after dynamic scaling and integer ratio tests, first section.

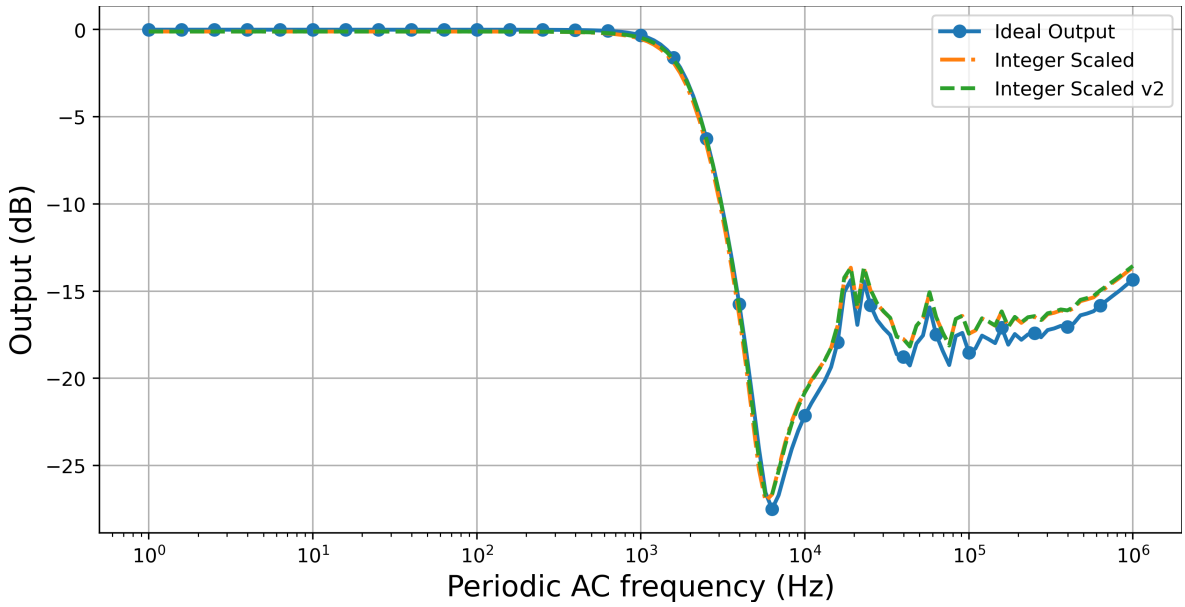

Figure 4.16. Butterworth low pass filter biquadratic sections magnitude responses after dynamic scaling and integer ratio tests, second section.

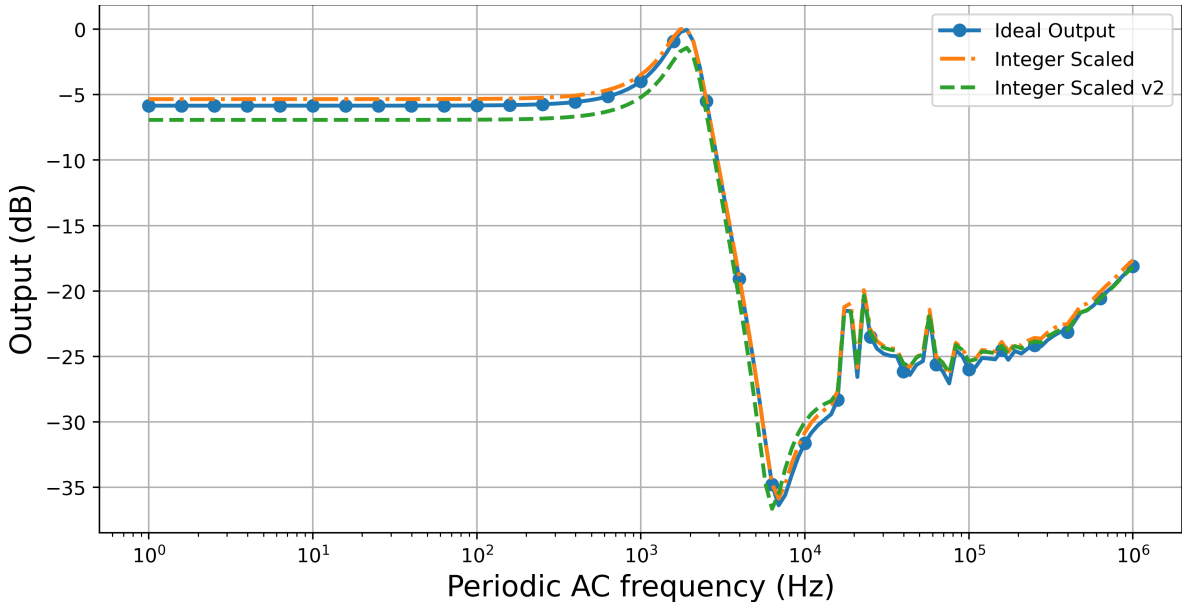

Figure 4.17. Butterworth low pass filter biquadratic sections magnitude responses after dynamic scaling and integer ratio tests,third section.

Table 4.6. Table for capacitance ratios for switched capacitor second order low pass filter (LPF) sections.

Variable name	**LPF Section 1**	**LPF Section 2**	**LPF Section 3**
C_1	8	14	6
C_2	8	14	11
C_A	26	30	20
C_4	24	24	6
C_3	24	24	13
C_{1pp}	2	3	1
C_B	9	16	16

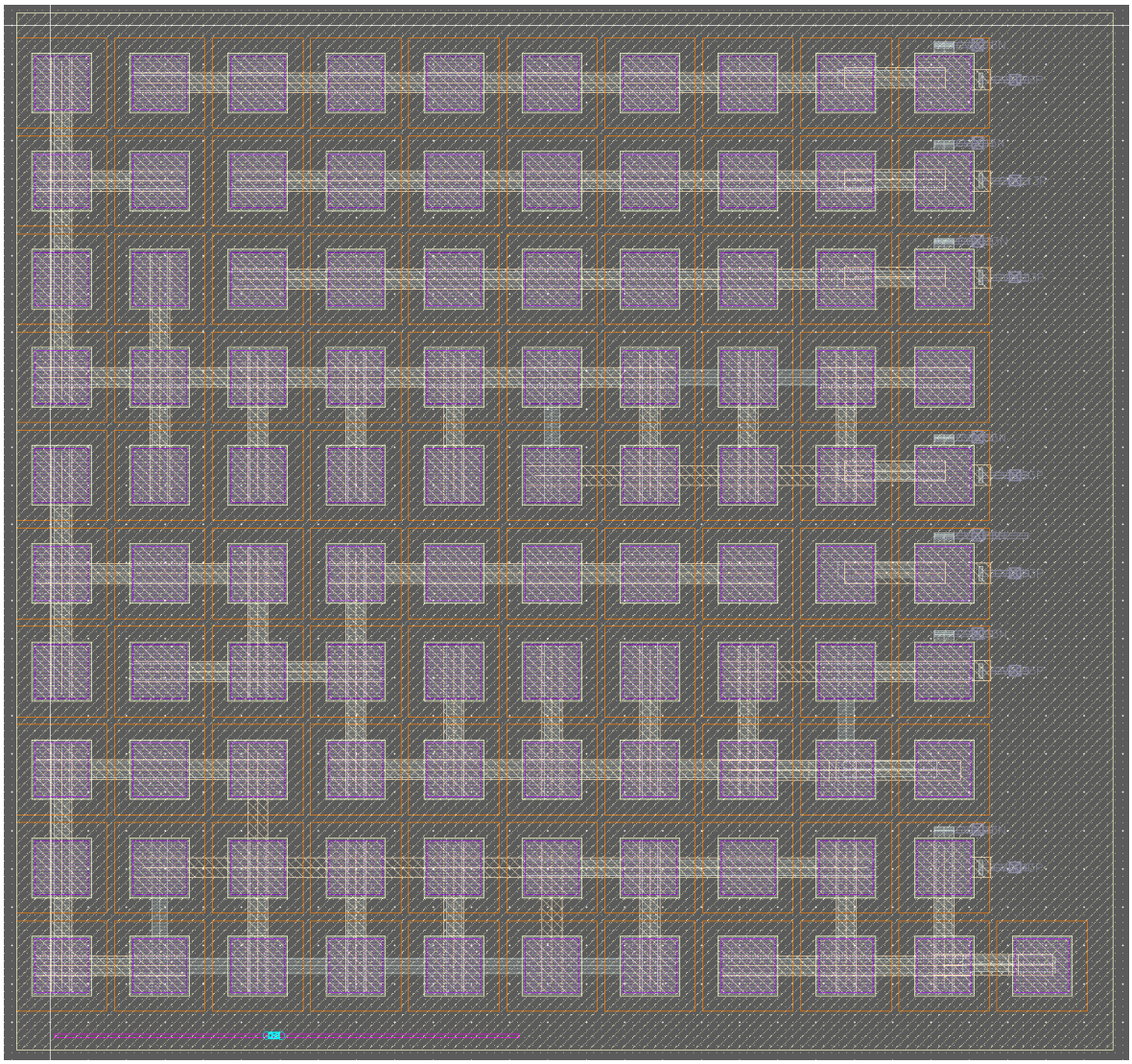

Figure 4.18. Layout of Butterworth low pass filter first section capacitors.

4.3.2. High Pass Filters

Similarly a sixth order Bessel high pass filter is designed. Ratio between cut off f_{-3db} and a clock frequency f_c will be 4/1000. If we use the same clock frequency of $f_c = 20kHz$ we can get a cut off frequency of $f_{-3db} = 80Hz$. Both of them have sections of low Q values so capacitor values are sized according to Table 3.2.

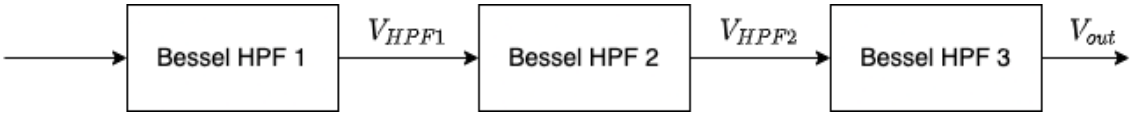

Figure 4.19. Bessel high pass filter second order sections.

Same procedure is followed as in the case of Butterworth low pass filter. Second order Bessel high pass filter Z transform values are tabulated in Table 4.7.

Table 4.7. Table for Bessel high pass filter second order stages before gain scaling and normalization.

	n_2	n_1	n_0	d_2	d_1	d_0
Stage 1	9.431e-1	-1.886e+0	9.431e-1	1.000e+0	-1.948e+0	9.483e-1
Stage 2	1.000e+0	-2.000e+0	1.000e+0	1.000e+0	-1.958e+0	9.588e-1
Stage 3	1.000e+0	-2.000e+0	1.000e+0	1.000e+0	-1.977e+0	9.780e-1

Similar to Butterworth low pass filter case, coefficients are gain scaled and normalized. New values are tabulated in Table 4.8.

Table 4.8. Table for Bessel high pass filter second order stages after gain scaling and normalization.

	n_2	n_1	n_0	d_2	d_1	d_0
Stage 1	1.034e+0	-2.068e+0	1.034e+0	1.054e+0	-2.054e+0	1.000e+0
Stage 2	1.023e+0	-2.046e+0	1.023e+0	1.043e+0	-2.042e+0	1.000e+0
Stage 3	1.003e+0	-2.006e+0	1.003e+0	1.023e+0	-2.022e+0	1.000e+0

Then, if we use Table 3.2 to find capacitor values of the circuit in Figure 3.23 for the high pass Bessel filter case, we would get the capacitor values presented in Table 4.9. Note that C_A and C_B capacitors have unit value of 1 and all of the rest are ratio values of capacitors with respect to unit value.

Table 4.9. Table for ideal output capacitance ratios for switched capacitor second order high pass filter (HPF) sections before scaling.

Variable name	**LPF Section 1**	**LPF Section 2**	**LPF Section 3**
C_1	0	0	0
C_2	0.0274	0.0260	0.0229
C_A	1	1	1
C_4	0.0545	0.0430	0.0225
C_3	0.0274	0.0260	0.0229
C_{1pp}	1.0341	1.0228	1.0028
C_B	1	1	1

A clear difference from low pass case is that C_1 capacitor value is 0 and it can be removed from the circuit in real implementation. After dynamic scaling, we would get the capacitance values of Table 4.10 in the case of Bessel high pass filters and simulation with the capacitance values of Table 4.10 with unit capacitor being 1 pF. If we look at the differences in before, Figure 4.20, and after ,Figure 4.21, dynamic scaling as done in the high pass case, we see in Figure 4.21 that first and second stages do not peak and have a slight change after dynamic scaling. First and second stage capacitance spread became worse after dynamic scaling since first and second stages were not peaking in the beginning. So, only the third stage will be dynamically scaled to preserve capacitor spread.

Table 4.10. Table for ideal output capacitance ratios for switched capacitor second order high pass filter (HPF) sections after dynamic scaling of all stages.

Variable name	**HPF Section 1**	**HPF Section 2**	**HPF Section 3**
C_1	0	0	0
C_2	0.02771	0.02607	0.02653
C_A	0.5139	0.6102	1.005
C_4	0.05504	0.0431	0.02607
C_3	0.0141	0.01586	0.02304
C_{1pp}	1.034	1.023	1.003
C_B	1.01	1.003	1.157

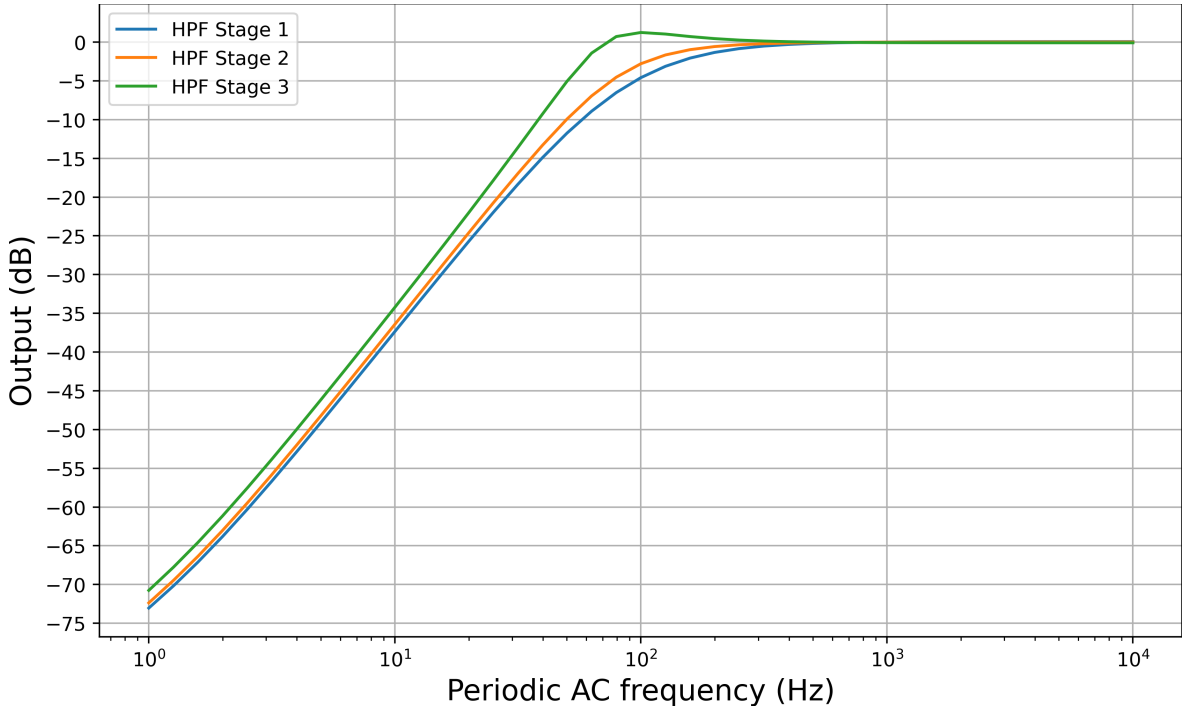

Figure 4.20. Bessel high pass filter second order section outputs before dynamic scaling.

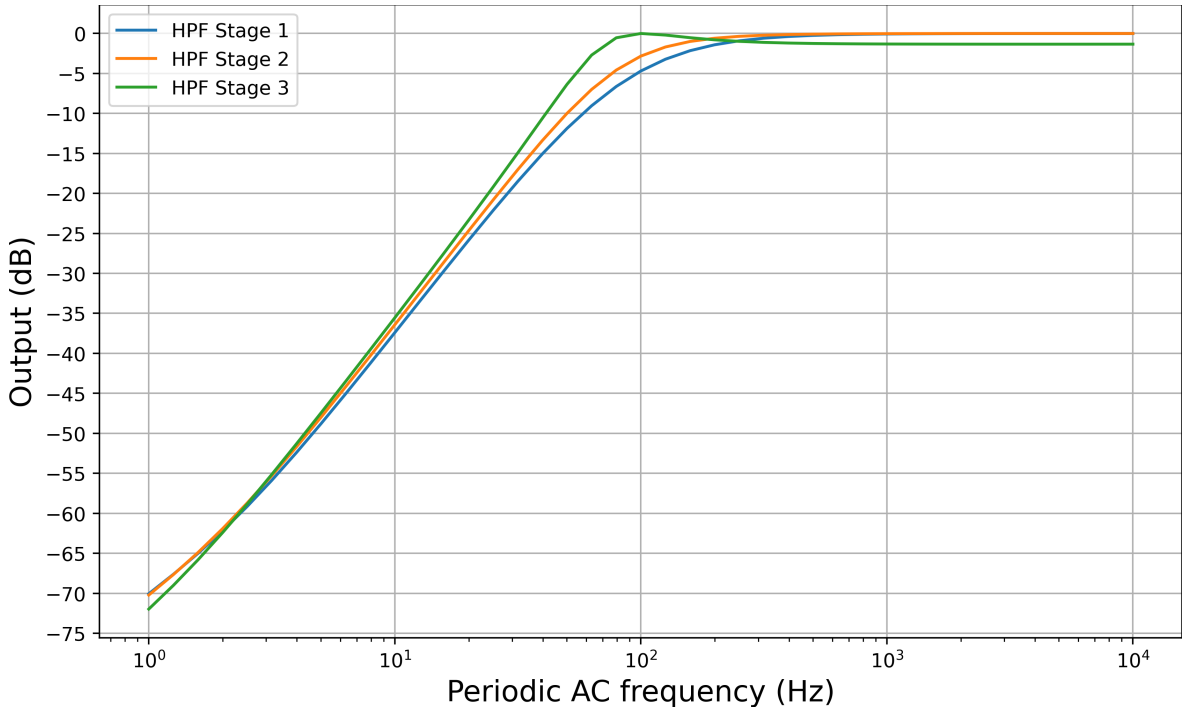

Figure 4.21. Bessel high pass filter second order section outputs after dynamic scaling.

Layout of a non-integer capacitor ratio will have problems in matching. A good practice is to have them in unit capacitors and have an integer ratio between them. Tests are done on low pass filters as seen in Figure 4.22, Figure 4.23 and Figure 4.24 to find optimal integer ratios. The most suitable integer ratios are listed in Table 4.11. Note that for the second stage a capacitor ratio of 1.5 is chosen since current capacitance spread is 50. Currently, if we use a unit capacitor of 100 fF, we would get a maximum capacitance of 5 pF. Scaling the second stage to an integer value would mean having a maximum capacitance value of 7.6 pF which is too large for the current operational amplifier to be able to have a safe operation in all common mode voltages. A 0.5 unit capacitor can be realized with a series connection of two unit capacitors.

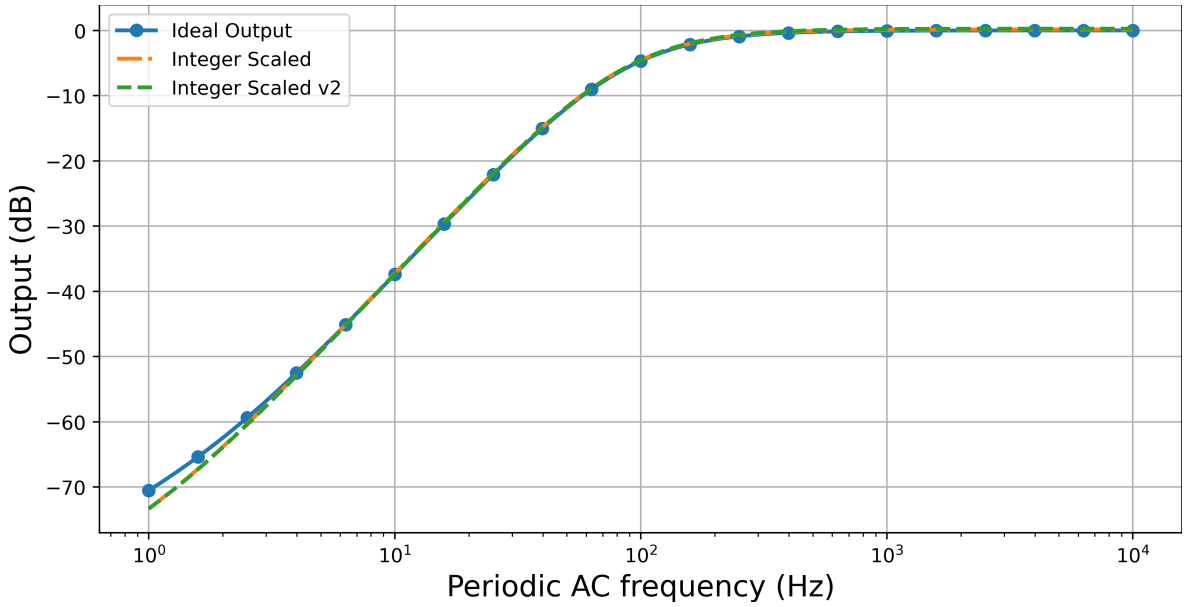

Figure 4.22. Bessel high pass filter biquadratic sections magnitude responses after dynamic scaling and integer ratio tests, first section.

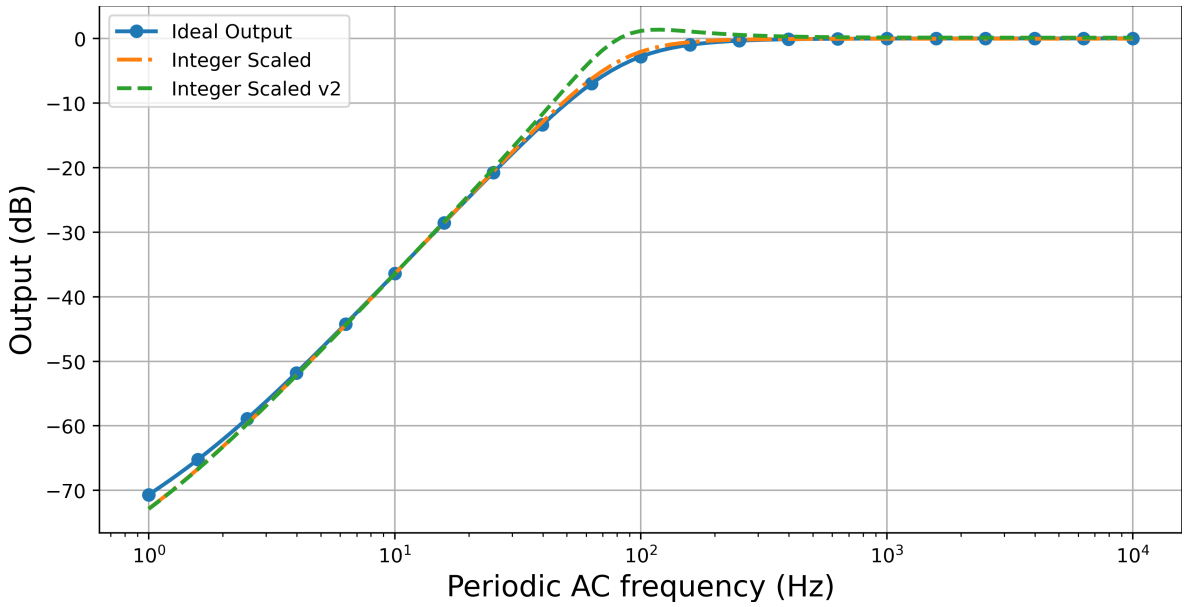

Figure 4.23. Bessel high pass filter biquadratic sections magnitude responses after dynamic scaling and integer ratio tests, second section.

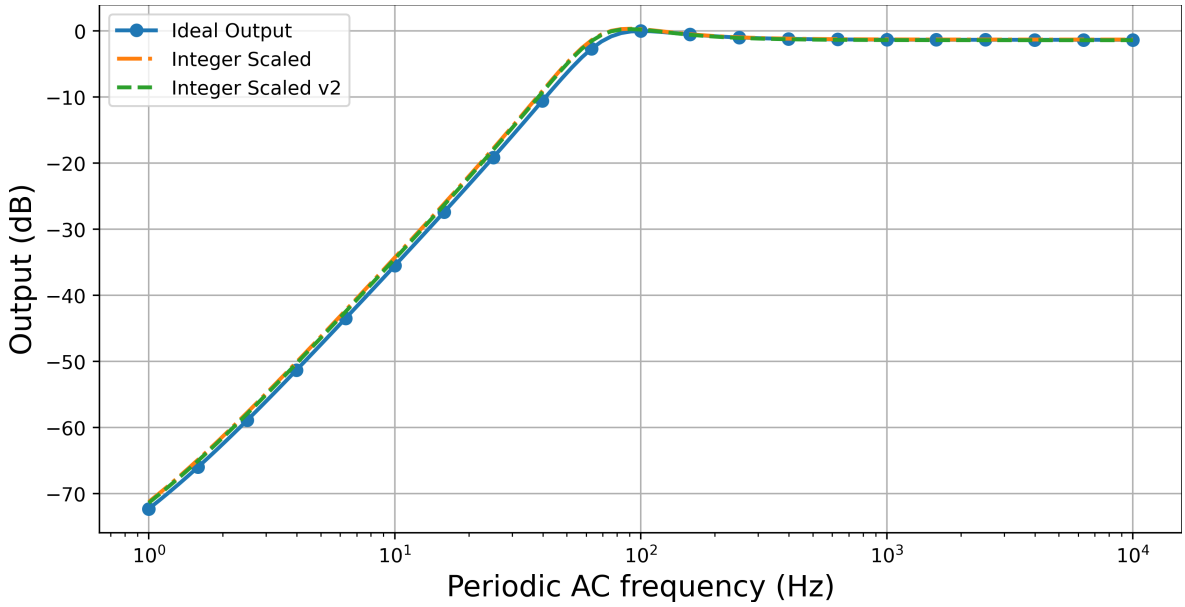

Figure 4.24. Bessel high pass filter biquadratic sections magnitude responses after dynamic scaling and integer ratio tests, third section.

Table 4.11. Table for capacitance ratios for switched capacitor second order high pass filter (HPF) sections.

Variable name	**HPF Section 1**	**HPF Section 2**	**HPF Section 3**
C_1	0	0	0
C_2	1	1	1
C_A	36	38	43
C_4	2	1.5	1
C_3	1	1	1
C_{1pp}	38	39	43
C_B	36	38	50

5. SIMULATION RESULTS

TSMC 180 nm 3.3/5 V high voltage process is used to design switched capacitor structures. To maintain simplicity, single ended circuits were designed and simulated. Supply voltage is chosen as 3V and a seperate reference voltage of 1.5 is assumed to be available from reference voltage generators. A clock signal of 20 kHz is used to drive non overlapping switches.

5.1. Low Pass Filter Simulations

For low pass filter stages depicted in Figure 5.1, periodic AC simulation results are shown below, where a maximally flat response with no ripples up to cut off frequency value is depicted in Figure 5.2.

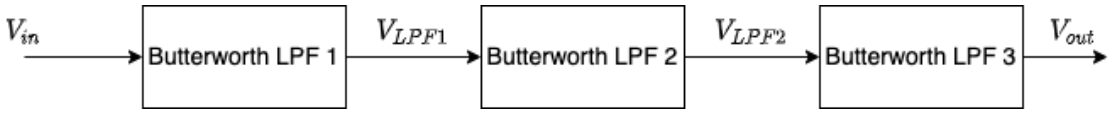

Figure 5.1. Butterworth low pass filter second order sections.

Implementation shows a cut off frequency of 1995 Hz which is very close to desired value. At 4000 Hz frequency, attenuation is found as -41.6 dB thus this filter has a roll off slope of nearly 39 db per octave which is much higher than CORSA specifications. Peaks can be seen at 20 kHz and multiples of it which are appearing from periodic AC simulation computation of Spectre simulator [76].

Group delay of the low pass filter is depicted in Figure 5.3. For the pass band up to 1 kHz, filters have a nearly constant delay of 0.3 ms. Since most of the adventitious sounds generated from lungs, especially fine crackles, have transient responses from 500-1000 Hz [17], those signals are not distorted from the peaking of the filter around cut off frequency. This also shows a design limitation of the minimum value of low pass filter cut off frequency in respiratory signal analysis.

Noise of the low pass sections are simulated with periodic noise (PNOISE) simulation with time domain analysis [76]. Result can be seen in Figure 5.4.

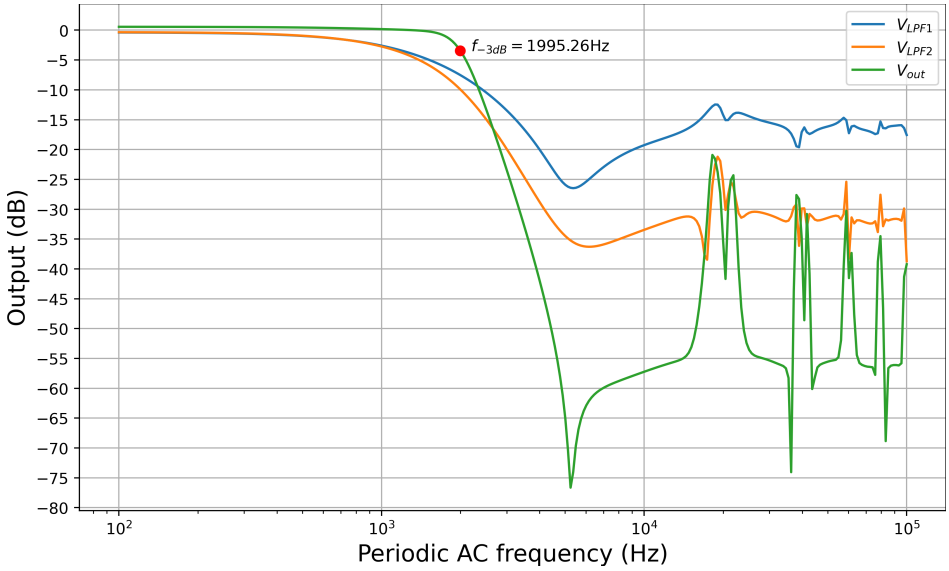

Figure 5.2. Butterworth low pass filter second order section periodic AC simulation results.

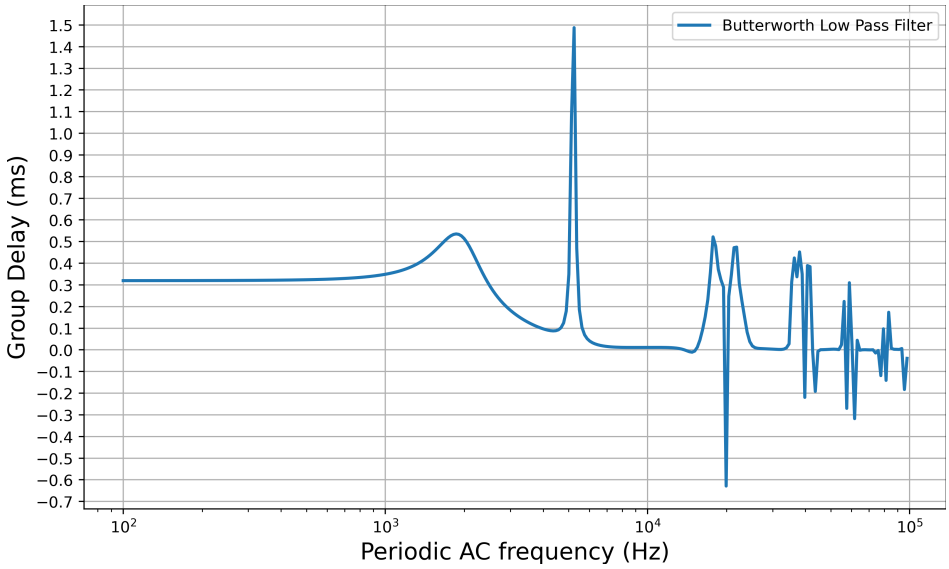

Figure 5.3. Butterworth sixth order low pass filter group delay from periodic AC simulation.

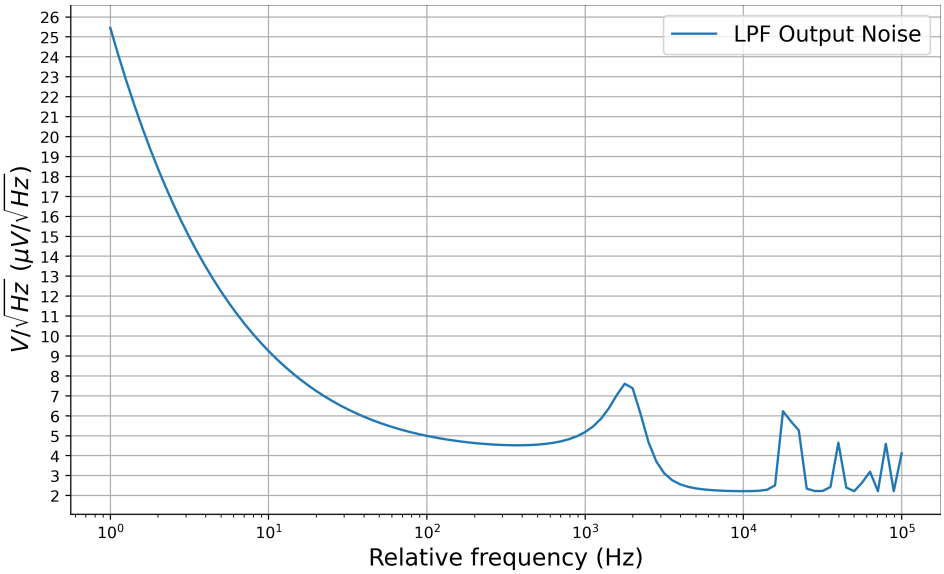

Figure 5.4. Butterworth sixth order low pass filter PNOISE simulation.

5.2. High Pass Filter Simulations

For high pass filter stages depicted in Figure 5.5, periodic AC simulation results are shown below, a ripple free flat band is generated from 125 Hz to nearly 20 kHz.

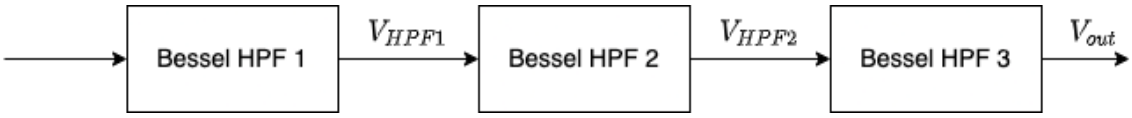

Figure 5.5. Bessel high pass filter second order sections.

Implementation shows a -3 db cut off frequency of 125.9 Hz but phase response simulation of the first stage shows that filter has -90 degree phase response at 85 Hz. Bessel implementation of Python in default sets cut off frequency of the signal as -90 degree phase point [73]. A phase measurement is shown in Figure 5.5 to show a -90 degree point. For the Bessel output, 63 Hz frequency point has -17 dB value thus a 14 dB per octave slope is obtained which is slightly lower than recommendation.

Group delay of the high pass filter is depicted in Figure 5.8. For the pass band from 300 Hz, the filter has no delay up to higher frequencies which helps in preserving transients of adventitious respiratory sounds [21].

Noise of the high pass sections are simulated with periodic noise (PNOISE) simulation with time domain analysis [76]. Result is depicted in Figure 5.9.

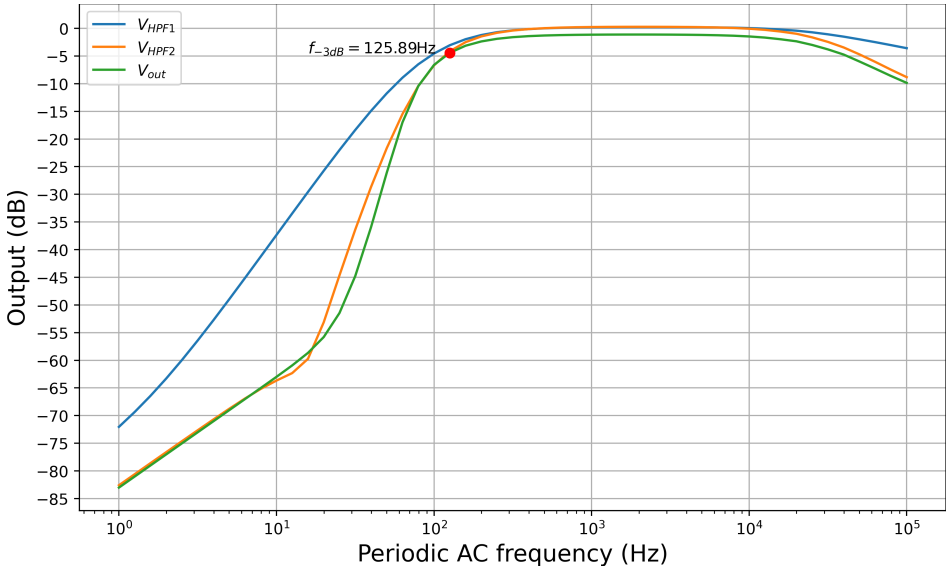

Figure 5.6. Bessel high pass filter second order section periodic AC simulation results.

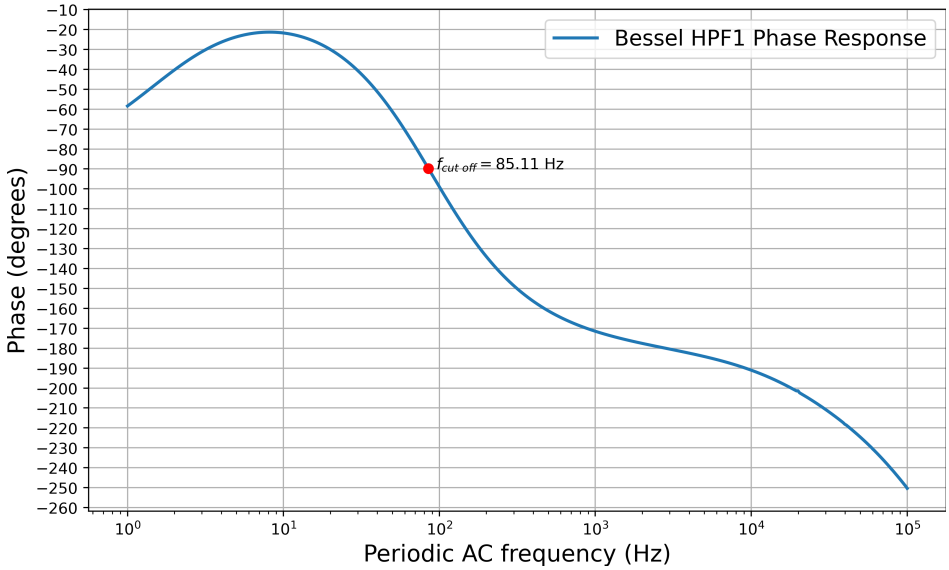

Figure 5.7. Bessel high pass filter first section phase response simulation results with -90 degree point.

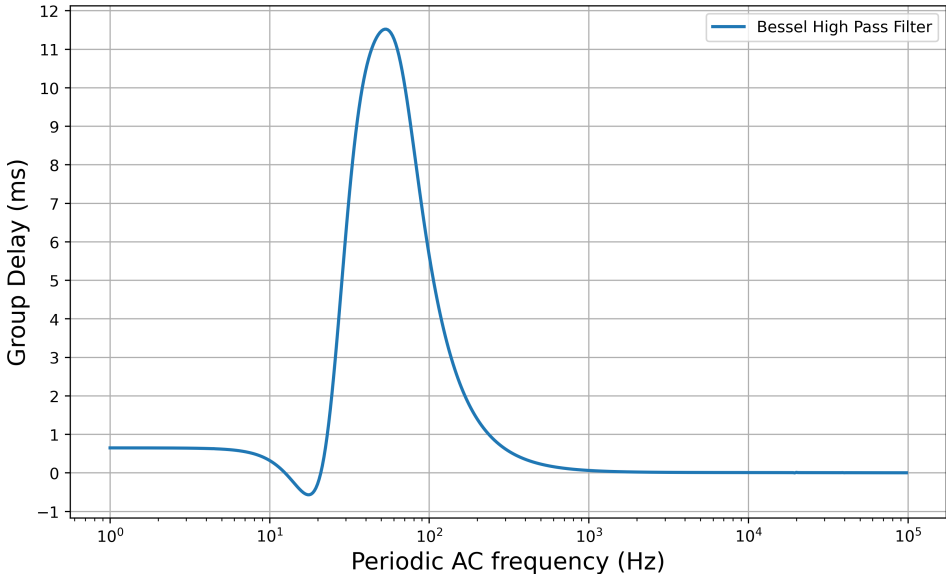

Figure 5.8. Bessel sixth order high pass filter group delay from periodic AC simulation.

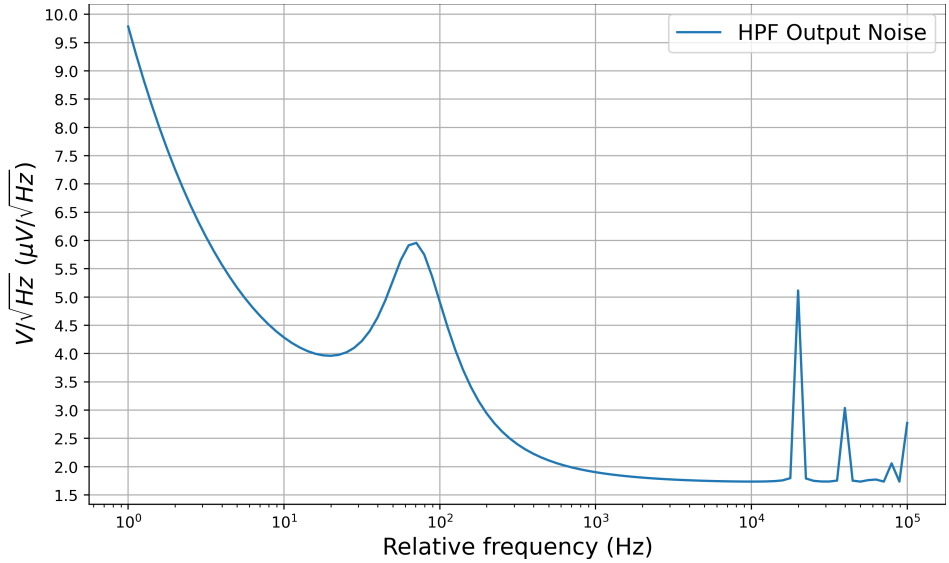

Figure 5.9. Bessel sixth order high pass filter PNOISE simulation.

5.3. Filters with Adjustable Cut Off

The switched capacitor filter structure has a significant advantage where cut-off frequency can be adjustable by changing switch clock signal frequency. The sixth order Butterworth low pass filter is simulated with three different switch frequencies of 20 kHz, 40 kHz and 80 kHz. Since this filter is designed to have a 1/10 ratio between cut-off and switching frequency, we see that in the Figure 5.10 cut-off frequencies of the filters are also scaled up with the same ratio. For a 20 kHz switching signal, cut off frequency is measured as 1995 Hz while ideal value should be 2000 Hz. For 40 kHz and 80 kHz switch signals, measured cut off values are 3891 and 7413 Hz respectively while ideal cut off values are 4000 Hz and 8000 Hz. A critical point in a low pass filter is the sampling frequency for ADC operation. Cut off frequency should be smaller than sampling frequency in a variable setting for this application since sampling frequency of the system is fixed. As an example, this system has a sampling frequency of 9600 Hz and variable cut off frequencies should not exceed that.

The sixth order Bessel high pass filter is also simulated with three different switch frequencies of 20 kHz, 40 kHz and 80 kHz. We see that in the Figure 5.11 cut-off frequencies of the filters are also scaled up with the same ratio. For 20 kHz switching signals, cut off frequency is measured as 132 Hz and for 40 kHz and 80 kHz switch signals, cut off values of 251 and 525 Hz are measured respectively.

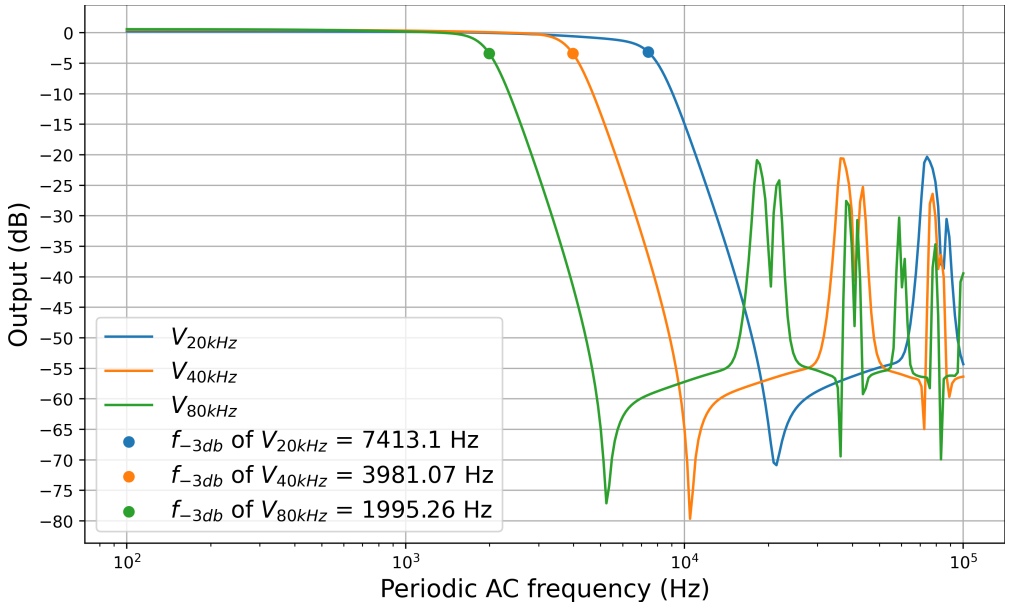

Figure 5.10. The sixth order Butterworth low pass filter periodic AC simulation results with switching frequencies of 20 kHz, 40 kHz and 80 kHz.

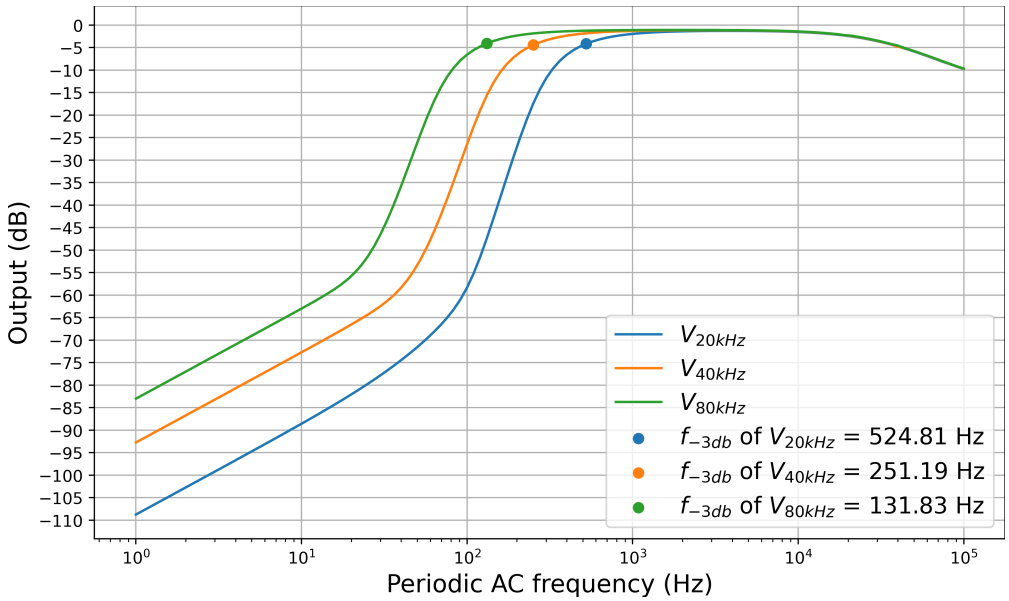

Figure 5.11. The sixth order Bessel high pass filter periodic AC simulation results with switching frequencies of 20 kHz, 40 kHz and 80 kHz.

6. CONCLUSION

In this work, a signal interfacing workflow for a future wearable respiratory data acquisition system is explained. Current methods to listen to respiratory sounds are investigated and electronic stethoscopes are listed. Due to imperfection of filter characteristics of electronic stethoscopes, CORSA task force initiated a standardization in computerized auscultation acquisition. By following those guidelines a list of low power MEMS analog microphones with flat responses are listed as a market research. Moreover, literature on acoustic coupling geometry of MEMS microscopes as in the electret microphones are presented and discussed. A variable gain stage with track and hold switched capacitors are presented as a proof of concept and ripple free low pass and high pass filter responses are realized with switched capacitor second order prototypes within good performance. A workflow of exact z-domain analysis of second order prototypes are presented and a rail to rail folded cascode operational amplifier is designed to be used in switched capacitor filter structures. Dynamic range scaling of capacitors and unit capacitor sizing is made without much compromise from filter characteristics. A partial layout of the components are presented and simulation results are shown. For future work, a differential gain and filter structure would be very beneficial since most of the differential analog MEMS microphones have better sensitivity from single ended ones and any common mode parasitic will be eliminated by differential process. Currently switched capacitor filter literature is more focused on low power neural data acquisition or always-on voice recognition with passive N path filters or gm-C filterbanks [77–81]. New classification algorithms that are pre trained on a specific sound could be a nice problem for those applications. If, full waveform of the auscultation data is still needed, biquad based switched capacitor filters are a good candidate for filtering.

REFERENCES

1. "WHO Coronavirus (COVID-19) Dashboard", 2021, `https://covid19.who.int/`, accessed on June 06, 2022.

2. Amore, S., E. Puppo, J. Melara, E. Terracciano, S. Gentili and G. Liotta, "Impact of COVID-19 on Older Adults and Role of Long-Term Care Facilities During Early Stages of Epidemic in Italy", *Scientific Reports*, Vol. 11, No. 1, pp. 1–13, 2021.

3. Alqahtani, J. S., T. Oyelade, A. M. Aldhahir, S. M. Alghamdi, M. Almehmadi, A. S. Alqahtani, S. Quaderi, S. Mandal and J. R. Hurst, "Prevalence, Severity and Mortality Associated With COPD and Smoking in Patients With COVID-19: a Rapid Systematic Review and Meta-analysis", *PLOS ONE*, Vol. 15, No. 5, pp. 1–13, 2020.

4. Ates, H. C., A. K. Yetisen, F. Güder and C. Dincer, "Wearable Devices for the Detection of COVID-19", *Nature Electronics*, Vol. 4, No. 1, pp. 13–14, 2021.

5. "Kry – Sjuksköterskor, Läkare och Psykologer", 2021, `https://www.kry.se/`, accessed on June 06, 2022.

6. "stethoscope — instrument — Britannica", 1998, `https://www.britannica.com/technology/stethoscope`, accessed on June 06, 2022.

7. "Laennec's Stethoscope — Science Museum Group Collection", 2002, `https://collection.sciencemuseumgroup.org.uk/objects/co90986/`, accessed on May 22, 2022 (CC BY-SA 4.0).

8. Wilks, S., "Abstract of Lecture on the Evolution of the Stethoscope", *The Lancet*, Vol. 120, No. 3091, pp. 882–883, 1882.

9. Kraman, S., G. Wodicka, G. Pressler and H. Pasterkamp, "Comparison of Lung Sound Transducers Using a Bioacoustic Transducer Testing System", *Journal of Applied Physiology*, Vol. 101, No. 2, pp. 469–476, 2006.

10. "The Brain in Space — NASA", 1998, `https://www.nasa.gov/audience/foreducators/topnav/materials/listbytype/The.Brain.in.Space.html`, accessed on May 28, 2022.

11. "3M™ Littmann® CORE Digital Stethoscope - Electronic Stethoscope — Eko", 2020, `https://www.littmann.com/3M/en_US/littmann-stethoscopes/advantages/core-digital-stethoscope`, accessed on June 01, 2022.

12. "Thinklabs ONE - Digital Stethoscope", 2003, `https://www.thinklabs.com/`, accessed on June 01, 2022.

13. "3M™ Littmann® Electronic Stethoscope Model 3200 3M Australia", 2001, `https://www.3m.com.au/3M/en_AU/p/d/b00037537`, accessed on June 06, 2022.

14. Khan, S. and V. Ahmed, "Investigation of Some Features for Preliminary Detection of Coronary Artery Disease Using Electronic Stethoscope", *International Conference on Emerging Trends in Communication Technologies (ETCT)*, 2016.

15. Abella, M., J. M. Formolo and D. G. Penney, "Comparison of the Acoustic Properties of Six Popular Stethoscopes", *The Journal of the Acoustical Society of America*, Vol. 91, No. 4, pp. 2224–2228, 1992.

16. Flietstra, B. C., N. Markuzon, A. Vyshedskiy and R. Murphy, "Automated Analysis of Crackles in Patients with Interstitial Pulmonary Fibrosis", *Pulmonary Medicine*, Vol. 1, No. 1, pp. 1–7, 2011.

17. Sen, I. and Y. Kahya, "A Multi-Channel Device for Respiratory Sound Data Acquisition and Transient Detection", *IEEE Engineering in Medicine and Biology 27th Annual Conference*, 2006.

18. Sovijarvi, A., J. Vanderschoot and J. Earis, "Standardization of Computerized Respiratory Sound Analysis", *European Respiratory Review*, Vol. 10, No. 77, pp. 585–585, 2000.

19. Sovijarvi, A., F. Dalmasso, J. Vanderschoot, L. Malmberg, G. Righini and S. Stoneman, "Definition of Terms for Applications of Respiratory Sounds", *European Respiratory Review*, Vol. 10, No. 77, pp. 597–610, 2000.

20. Rossi, M., A. Sovijarvi, P. Piirila, L. Vannuccini, F. Dalmasso and J. Vanderschoot, "Environmental and Subject Conditions and Breathing Manoeuvres for Respiratory Sound Recordings", *European Respiratory Review*, Vol. 10, No. 77, pp. 611–615, 2000.

21. Vannuccini, L., J. Earis, P. Helisto, B. Cheetham, M. Rossi, A. Sovijarvi and J. Vanderschoot, "Capturing and Preprocessing of Respiratory Sounds", *European Respiratory Review*, Vol. 10, No. 77, pp. 616–620, 2000.

22. Cheetham, B., G. Charbonneau, A. Giordano, P. Helisto and J. Vanderschoot, "Digitization of Data for Respiratory Sound Recordings", *European Respiratory Review*, Vol. 10, No. 77, pp. 621–624, 2000.

23. Earis, J. and B. Cheetham, "Future Perspectives for Respiratory Sound Research", *European Respiratory Review*, Vol. 10, No. 77, pp. 641–646, 2000.

24. Piirila, P., A. Sovijarvi, J. Earis, M. Rossi, F. Dalmasso, S. Stoneman and J. Vanderschoot, "Reporting Results of Respiratory Sound Analysis", *European Respiratory Review*, Vol. 10, No. 77, pp. 636–640, 2000.

25. Earis, J. and B. Cheetham, "Current Methods Used for Computerized Respiratory Sound Analysis", *European Respiratory Review*, Vol. 10, No. 77, pp. 586–590, 2000.

26. Sovijarvi, A., "Characteristics of Breath Sounds and Adventitious Respiratory Sounds", *European Respiratory Review*, Vol. 10, No. 77, pp. 591–596, 2000.

27. Murphy, R. L., A. Vyshedskiy, V.-A. Power-Charnitsky, D. S. Bana, P. M. Marinelli, A. Wong-Tse and R. Paciej, "Automated Lung Sound Analysis in Patients with Pneumonia", *Respiratory Care*, Vol. 49, No. 12, pp. 1490–1497, 2004.

28. Kahya, Y. P., S. Yerer and O. Cerid, "A Wavelet-Based Instrument for Detection of Crackles in Pulmonary Sounds", *Conference Proceedings of the 23rd Annual International Conference of the IEEE Engineering in Medicine and Biology Society*, 2001.

29. Oliveira, A., I. Sen, Y. P. Kahya, V. Afreixo and A. Marques, "Computerised Respiratory Sounds can Differentiate Smokers and Non-Smokers", *Journal of Clinical Monitoring and Computing*, Vol. 31, No. 1, pp. 571–580, 2016.

30. Moussavi, Z., M. T. Leopando, H. Pasterkamp and G. Rempel, "Computerised Acoustical Respiratory Phase Detection without Airflow Measurement", *Medical and Biological Engineering and Computing*, Vol. 38, No. 1, pp. 198–203, 2006.

31. Klum, M., F. Leib, C. Oberschelp, D. Martens, A.-G. Pielmus, T. Tigges, T. Penzel and R. Orglmeister, "Wearable Multimodal Stethoscope Patch for Wireless Biosignal Acquisition and Long-Term Auscultation", *41st Annual International Conference of the IEEE Engineering in Medicine and Biology Society (EMBC)*, 2019.

32. "Digital Medical Devices. Innovative Technology — Ekuore", 2021, `https://ekuore.com`, accessed on June 07, 2022.

33. "Steth IO - Next Generation Telemedicine Platform", 2022, `https://stethio.com/`, accessed on June 07, 2022.

34. Kahya, Z. Y. and I. Sen, "Auscultation Data Acquisition, Communication and Evaluation System Incorporating Mobile Facilities", U.S. Patent 20170071565 A1, 21 July 2020, `https://patents.google.com/patent/US20170071565A1`, accessed on June 06, 2022.

35. "A Smart Way of Asthma Monitoring", 2022, https://www.stethome.com/en-gb/, accessed on June 07, 2022.

36. "Eko DUO ECG + Digital Stethoscope", 2022, https://shop.ekohealth.com/products/duo-ecg-digital-stethoscope?variant=39350415655008, accessed on June 07, 2022.

37. "Stemoscope – Listen to the Sound of Life, more than an Electronic Stethoscope or a Digital Stethoscope", 2022, https://www.stemoscope.com/, accessed on June 07, 2022.

38. "Smart Stethoscope — Digital Bluetooth Stethoscope — Feelix — Sonavilabs", 2022, https://sonavilabs.com/, accessed on June 07, 2022.

39. Yilmaz, G., M. Rapin, D. Pessoa, B. M. Rocha, A. M. de Sousa, R. Rusconi, P. Carvalho, J. Wacker, R. P. Paiva and O. Chételat, "A Wearable Stethoscope for Long-Term Ambulatory Respiratory Health Monitoring", *Sensors*, Vol. 20, No. 18, pp. 1 – 14, 2020.

40. Lee, K., X. Ni, J. Y. Lee, H. M. Arafa, D. J. Pe, S. Xu, R. Avila, M. Irie, J. Lee, R. Easterlin, D. H. Kim, H. U. Chung, O. O. Olabisi, S. Getaneh, E. Chung, M. Hill, J. Bell, H. Jang, C. Liu, J. B. Park, J. Kim, S. B. Kim, S. Mehta, M. Pharr, A. Tzavelis, J. T. Reeder, I. Huang, Y. Deng, Z. Xie, C. Davies, Y. Huang and J. A. Rogers, "Mechanoacoustic Sensing of Physiological Processes and Body Motions via a Soft Wireless Device Placed at the Suprasternal Notch", *Nature Biomedical Engineering*, Vol. 4, No. 1, pp. 148 – 158, 2019.

41. Klum, M., M. Urban, T. Tigges, A.-G. Pielmus, A. Feldheiser, T. Schmitt and R. Orglmeister, "Wearable Cardiorespiratory Monitoring Employing a Multimodal Digital Patch Stethoscope: Estimation of ECG, PEP, LVET and Respiration Using a 55 mm Single-Lead ECG and Phonocardiogram", *Sensors*, Vol. 20, No. 7, pp. 1 – 21, 2020.

42. Cotur, Y., M. Kasimatis, M. Kaisti, S. Olenik, C. Georgiou and F. Güder, "Stretchable Composite Acoustic Transducer for Wearable Monitoring of Vital Signs", *Advanced Functional Materials*, Vol. 30, No. 16, pp. 1910288–1910295, 2020.

43. Panda, B., S. Mandal and S. J. A. Majerus, "Flexible, Skin Coupled Microphone Array for Point of Care Vascular Access Monitoring", *IEEE Transactions on Biomedical Circuits and Systems*, Vol. 13, No. 6, pp. 1494–1505, 2019.

44. Rayburn, R. A., *Eargle's The Microphone Book: From Mono to Stereo to Surround - A Guide to Microphone Design and Application, Third Edition*, Routledge, New York, 2011.

45. Tilli, M., M. Paulasto-Krockel, M. Petzold, H. Theuss, T. Motooka and V. Lindroos, *Handbook of Silicon Based MEMS Materials and Technologies*, Elsevier, Amsterdam, Netherlands, 2020.

46. "AirPods Pro Teardown - iFixit", 2019, `https://www.ifixit.com/Teardown/AirPods+Pro+Teardown/127551`, accessed on June 07, 2022.

47. "Knowles", 2022, `https://www.knowles.com/`, accessed on June 07, 2022.

48. "High SPL Analog Microphone with Extended Low Frequency Response", 2019, `https://invensense.tdk.com/wp-content/uploads/2019/02/DS-ICS-40300-00-v1.3.pdf?ref_disty=digikey`, accessed on May 24, 2022.

49. "Analog Bottom Port Sisonic™ Microphone", 2022, `https://eu.mouser.com/datasheet/2/218/Knowles_Corporation_SPH8878LR5H_1_Lovato_Datasheet-2492662.pdf`, accessed on May 24, 2022.

50. "AEC-Q103 Qualified Analog Bottom Port Sisonic™ Microphone", 2021, `https://www.knowles.com/docs/default-source/model-downloads/sph1878lr5h-1_datasheet.pdf`, accessed on May 26, 2022.

51. "Analog Bottom Port Sisonic™ Microphone", 2021,

https://www.knowles.com/docs/default-source/model-downloads/spv08a0lr5h-1-datasheet-rev-a.pdf, accessed on May 26, 2022.

52. "CUI Devices, Model: CMM-2718AB-3815NC-TR", 2020, https://www.cuidevices.com/product/resource/cmm-2718ab-3815nc-tr.pdf, accessed on May 26, 2022.

53. "Knowles Versatile, High-Performance, Multi-Mode Analog Microphone", 2022, https://www.knowles.com/docs/default-source/default-document-library/spw0878lr5h-1_ellen_product_brief.pdf, accessed on May 26, 2022.

54. "CUI Devices Model: CMM-2718AT-3817NC-TR", 2020, https://www.cuidevices.com/product/resource/cmm-2718at-3817nc-tr.pdf, accessed on May 26, 2022.

55. "Data Sheet AMM-2742-T-R", 2020, https://www.puiaudio.com/media/SpecSheet/AMM-2742-T-R.pdf, accessed on May 26, 2022.

56. "Data Sheet AMM-3742-T-WP-R", 2021, https://www.puiaudio.com/media/SpecSheet/AMM-3742-T-WP-R.pdf, accessed on May 26, 2022.

57. "3M™ Littmann® Classic III™ Stethoscope — 3M United States", 2000, https://www.littmann.com/3M/en_US/littmann-stethoscopes/products/~/3M-Littmann-Classic-III-Stethoscope/, accessed on May 26, 2022.

58. Alsmadi, S. and Y. P. Kahya, "Design of a DSP-Based Instrument for Real-Time Classification of Pulmonary Sounds", *Computers in Biology and Medicine*, Vol. 38, No. 1, pp. 53–61, 2008.

59. Kraman, S. S., G. R. Wodicka, Y. Oh and H. Pasterkamp, "Measurement of Respiratory Acoustic Signals. Effect of Microphone Air Cavity Width, Shape, and Venting", *Chest*, Vol. 108, No. 4, pp. 1004–1008, 1995.

60. "MEMS Microphone Mechanical & Acoustical Implementation", 2018,

https://www.infineon.com/dgdl/Infineon-AN557_MEMS_microphone_mechanical_and_acoustical_implementation-AN-v01_01-EN.pdf, accessed on June 07, 2022.

61. "MEMS Microphone Guide - Mosomic", 2021, http://www.mosomic.com/mems-microphone-guide/, accessed on June 07, 2022.

62. Sühn, T., M. Spiller, R. Salvi, S. Hellwig, A. Boese, A. Illanes and M. Friebe, "Auscultation System for Acquisition of Vascular Sounds Towards Sound-Based Monitoring of the Carotid Artery", *Medical Devices*, Vol. 13, No. 1, pp. 349–364, 2020.

63. Sühn, T., A. Sreenivas, N. Mahmoodian, I. M. Zambrano, A. Boese, A. Illanes, M. Bloxton and M. Friebe, "Design of an Auscultation System for Phonoangiography and Monitoring of Carotid Artery Diseases", *41st Annual International Conference of the IEEE Engineering in Medicine and Biology Society (EMBC)*, 2019.

64. "Simulation Software for Analyzing Acoustics and Vibrations", 2021, https://www.comsol.com/acoustics-module, accessed on June 07, 2022.

65. Yen, R. C. and P. R. Gray, "A MOS Switched-Capacitor Instrumentation Amplifier", *IEEE Journal of Solid-State Circuits*, Vol. 17, No. 6, pp. 1008–1013, 1982.

66. Wakaumi, H., "A Switched-Capacitor Filter with Dynamic Switching Bias OP Amplifiers", *IEEE 8th Latin American Symposium on Circuits & Systems (LASCAS)*, 2017.

67. Steyaert, M. S. J. and W. M. C. Sansen, "A Micropower Low-Noise Monolithic Instrumentation Amplifier for Medical Purposes", *IEEE Journal of Solid-state Circuits*, Vol. 22, No. 6, pp. 1163–1168, 1987.

68. Harb, A. and M. Sawan, "New Low-Power Low-Voltage High-CMRR CMOS In-

strumentation Amplifier", *Proceedings of the IEEE International Symposium on Circuits and Systems VLSI*, 1999.

69. Yoshizawa, H. and G. C. Temes, "Switched-Capacitor Track-and-Hold Amplifiers With Low Sensitivity to Op-Amp Imperfections", *IEEE Transactions on Circuits and Systems I: Regular Papers*, Vol. 54, No. 1, pp. 193–199, 2007.

70. Williams, A. B. and F. J. Taylor, *Electronic Filter Design Handbook*, McGraw-Hill Education, New York, 2006.

71. "scipy.signal.butter — SciPy v1.8.1 Manual", 2019, `https://docs.scipy.org/doc/scipy/reference/generated/scipy.signal.butter.html`, accessed on June 07, 2022.

72. "Active and Passive Filter Designer", 2019, `http://www.spectrum-soft.com/demo/filter.shtm`, accessed on June 07, 2022.

73. Virtanen, P., R. Gommers, T. E. Oliphant, M. Haberland, T. Reddy, D. Cournapeau, E. Burovski, P. Peterson, W. Weckesser, J. Bright, S. J. van der Walt, M. Brett, J. Wilson, K. J. Millman, N. Mayorov, A. R. J. Nelson, E. Jones, R. Kern, E. Larson, C. J. Carey, İ. Polat, Y. Feng, E. W. Moore, J. VanderPlas, D. Laxalde, J. Perktold, R. Cimrman, I. Henriksen, E. A. Quintero, C. R. Harris, A. M. Archibald, A. H. Ribeiro, F. Pedregosa, P. van Mulbregt and SciPy 1.0 Contributors, "SciPy 1.0: Fundamental Algorithms for Scientific Computing in Python", *Nature Methods*, Vol. 17, No. 1, pp. 261–272, 2020.

74. Maxwell, J. C., "A Treatise on Electricity and Magnetism", *Nature*, Vol. 7, No. 1, pp. 478–480, 1873.

75. Gregorian, R. and G. C. Temes, *Analog MOS Integrated Circuits for Signal Processing*, Wiley, New York, 1986.

76. Kundert, K. S., "Simulating Switched-Capacitor Filters with SpectreRF", 2001, `https://designers-guide.org/analysis/sc-filters.pdf`, accessed on June 07, 2022.

77. Shi, E., X. Tang and K. P. Pun, "A 270 nW Switched-Capacitor Acoustic Feature Extractor for Always-On Voice Activity Detection", *IEEE Transactions on Circuits and Systems I: Regular Papers*, Vol. 68, No. 3, pp. 1045–1054, 2021.

78. Badami, K. M. H., V. R. Pamula and M. Verhelst, "A Switched-Capacitor Degenerated, Scalable gm-C Filter-Bank for Acoustic Front-Ends", *IEEE International Symposium on Circuits and Systems (ISCAS)*, 2016.

79. Villamizar, D. A., *Low Power Audio Feature Extraction for Machine Learning Applications*, Ph.D. Thesis, Stanford University, 2021.

80. Villamizar, D. A., D. G. Muratore, J. B. Wieser and B. Murmann, "An 800 nW Switched-Capacitor Feature Extraction Filterbank for Sound Classification", *IEEE Transactions on Circuits and Systems I: Regular Papers*, Vol. 68, No. 4, pp. 1578–1588, 2021.

81. Villamizar, D. A., D. Battaglino, D. G. Muratore, R. Hoshyar and B. Murmann, "Sound Classification using Summary Statistics and N-Path Filtering", *IEEE International Symposium on Circuits and Systems (ISCAS)*, 2019.